IOP Publishing Plasma Sources Sci. Technol. 35 (2026) 035011 https://doi.org/10.1088/1361-6595/ae4d04

Plasma Sources Science and Technology

OPEN ACCESS

RECEIVED
20 November 2025

REVISED
3 February 2026

ACCEPTED FOR PUBLICATION
3 March 2026

PUBLISHED
16 March 2026

PAPER

Modeling remote inductively coupled plasmas for plasma-enhanced atomic layer deposition

Mackenzie E Meyer[1], **David R Boris**[2], **Michael J Johnson**[2], **Mark J Kushner**[3] **and Scott G Walton**[2,*]

[1] NRC Postdoctoral Research Associate, Plasma Physics Division, US Naval Research Laboratory, Washington, DC, United States of America
[2] Plasma Physics Division, US Naval Research Laboratory, Washington, DC, United States of America
[3] Electrical Engineering & Computer Science Department, University of Michigan, Ann Arbor, MI, United States of America
[*] Author to whom any correspondence should be addressed.

E-mail: scott.g.walton.civ@us.navy.mil

Keywords: plasma-enhanced atomic layer deposition, modeling, Langmuir probe, remote plasma source, inductively coupled plasma

Abstract

Remote inductively coupled plasmas (ICPs) are utilized in atomic precision processing as they provide the requisite flux of reactive and energetic species. Their remote nature helps mitigate damage to the substrate by energetic ions and photons produced in the plasma. However, the attributes of these plasma sources are not well characterized, particularly in the spatial afterglow where the growth substrate is located. This work focuses on modeling a commercially available remote ICP source with a 2D hybrid plasma model in pure Ar. The results of the model are benchmarked against spatially resolved Langmuir probe measurements in Ar and achieve good agreement with the measurements in the afterglow for a variety of operating conditions. The benchmarked results provide confidence in the model, which can then be used to better understand the physics in the spatial afterglow. In the remote ICP system, capacitive power coupling plays a large role in determining the plasma properties in the spatial afterglow, where a small amount of capacitive power coupling is responsible for elevated electron density, plasma potential, and electron temperature. These results are discussed in the context of atomic layer deposition (ALD). While this work discusses pure Ar plasmas, capacitive power coupling in the afterglow will affect mixtures with molecular gases used in ALD.

1. Introduction

Low-temperature plasmas (LTPs) have long been used extensively in semiconductor manufacturing [1, 2]. More recently, LTPs have found increasing utility in atomic layer deposition (ALD) processes due to their unique chemistries and near ambient operating temperatures [3–6]. These properties allow for the development of novel materials and processing of thermally sensitive compounds. While advantageous, LTPs deliver a flux of species and energy to the substrate that must be understood and controlled to achieve the required atomic layer precision.

Reactive neutrals, ions, and photons produced in the plasma are typically the species that drive the plasma-enhanced ALD (PEALD) process at the substrate. However, energetic species produced in the plasma can lead to etching and the production of chemical or structural defects in the growing film. The ions in particular can deliver a significant amount of energy to the substrate as ions gain energy by accelerating through the sheath above the substrate. Using a remote plasma configuration, where the substrate is placed far from the plasma source in the spatial afterglow of the plasma, can minimize this energy delivery and therefore minimize damage to the substrate. Since the density of ions rapidly decreases outside the plasma source, the ion flux and therefore energy delivered to the substrate is limited. The decay of reactive neutrals is less dramatic since they have longer lifetimes than the ions.

Therefore, chemically active species can be delivered to the substrate while minimizing the damage associated with a large flux of energetic ions. Still, many questions remain about the operation of remote plasma sources and their underlying plasma physics.

Previous studies have examined remote plasma configurations and their applications in PEALD [7–11]. Properties of the remote plasma have been investigated through modeling and experimental measurements. Li *et al* showed the importance of nonlocal electron kinetics in the operation of a remote inductively coupled plasma (ICP) formed in low pressure Ar through both Langmuir probe measurements and hybrid modeling [12]. Tinck and Bogaerts modeled a remote ICP in O_2 for various powers and pressures and examined ion and radical densities as a function of position in the reactor [13]. Gao *et al* measured electron energy distribution functions (EEDFs) for H_2 remote plasmas, showing they evolved to a Maxwellian distribution in the afterglow [14]. Gao *et al* also showed stochastic heating dominated at low pressures [15]. Jo and Kim modeled a remote ICP in Ar and benchmarked the electron density against Langmuir probe measurements [16]. They also showed increasing the gas flow rate increased the ion flow downstream of the ICP. Cheon *et al* used a detailed reaction mechanism to determine dominant reactions in an Ar remote ICP and found stepwise ionization was important at pressures higher than 1 Torr [17]. Huang *et al* modeled a remote capacitively coupled plasma and showed a relatively high electron density a few cm downstream of the plasma [18]. At high powers, energetic electrons in the afterglow contribute to electron production via ionization. The studies that examined the afterglow show the decrease in electron density and potential in the spatial afterglow [12–16, 18], which does serve to limit the energy delivered to the substrate as discussed above. However, there has been little emphasis on the effect of power coupling downstream of the source in a remote ICP system.

In this work, we characterize the properties of a commercially available remote ICP and the associated spatial afterglow with a 2D hybrid plasma model. The modeling is motivated by previous measurements of remote ICP systems performed at the US Naval Research Laboratory that raised questions about the role of capacitive power coupling in the afterglow [19]. In particular, the plasma potential in the afterglow is elevated, possibly leading to high ion energies at the substrate. Additionally, a power coupling transition between H-mode and E-mode was observed and accompanied by an abrupt change in optical emission from the plasma as well as a reduction in the atomic N produced in the plasma that is required for PEALD of metal nitrides. As such, we focus on the role that capacitive power coupling plays in this system, particularly in the spatial afterglow. To achieve this goal, a remote ICP sustained in Ar was simulated with a 2D hybrid plasma model and benchmarked against experimental measurements at a variety of operating conditions. We use the model results to examine the dominant physical processes to better understand the physics of remote ICPs with a focus on the spatial afterglow.

While the pure Ar plasmas investigated in this work are not typically used for PEALD, pure Ar plasmas have been shown to crystalize films in atomic layer annealing (ALA) processes [20–22]. ALA is typically incorporated as an additional step in the ALD cycle, where an inert plasma delivers energy to the top few monolayers of the substrate with the intent of developing a crystalline structure. The relevant results of this work will be discussed within this context in addition to PEALD.

This paper is structured as follows. In section 2, descriptions of the remote ICP system, model, and experimental measurements are given. In section 3, the base case is analyzed and benchmarked against experimental measurements. Variations in plasma properties with pressure and power are examined and benchmarked against measurements in section 4. Implications of these results for PEALD are discussed in section 5. Concluding remarks are presented in section 6.

2. Description of model and experiments

The remote ICP source used in this study is the Veeco Fiji G2 and is shown in figure 1. The source is mounted on a custom-built chamber with sufficient access to incorporate plasma diagnostics into the spatial afterglow. The source utilizes a 17 cm long, 10 turn solenoidal coil wrapped around a sapphire tube. The operational pressure range of the Veeco Fiji G2 is nominally 1 mTorr–1 Torr. The grounded end of the coil is near the gas inlet at the top of the reactor, while the powered end of the coil is near the exit of the ICP into the larger downstream chamber. A range of powers from 50 W–300 W are supplied by a Seren R301 RF amplifier at 13.56 MHz. A Seren AT-3 matchbox is used between the power supply and the coil to minimize the reflected power by matching the impedance of the plasma to that of the coil. The reflected power was less than 1% of the forward power for these conditions. The sapphire tube has an inner diameter of 3.49 cm (1.75 cm radius) and an outer diameter of 3.81 cm. The diagnostics chamber is an 8 inch Conflat 6 way cross. A grounded cylindrical mesh is inserted to match the cylindrically symmetric geometry in the model.

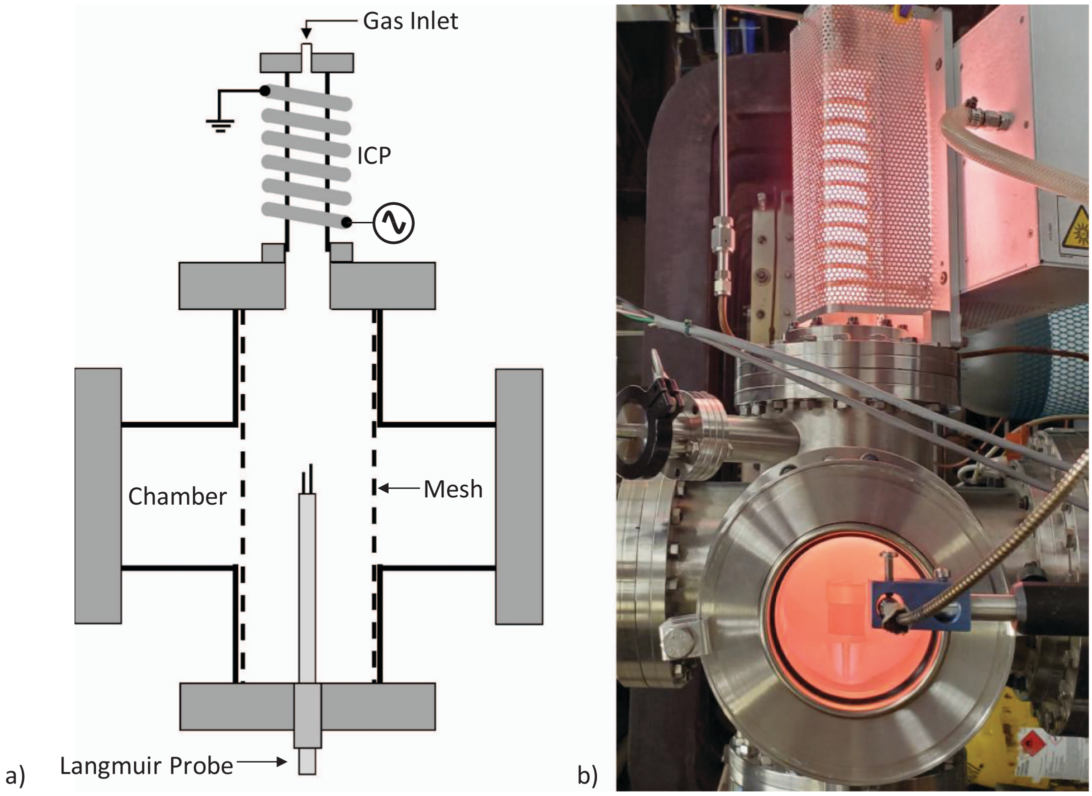

Figure 1. Veeco Fiji G2 source and diagnostics chamber. (a) Schematic diagram (not to scale) of the ICP source and diagnostic chamber and (b) photograph of the source and chamber.

2.1. Description of the model

The model used in this work is the 2D hybrid plasma equipment model (HPEM), described in detail in [23–26]. HPEM uses time slicing algorithms to span the wide range of relevant timescales in the plasma from electromagnetics (10s of ps) to fluid flow ($>$ ms). The modules of HPEM used in this study include the electromagnetics module (EMM), electron energy transport module (EETM), and fluid kinetics-Poisson module (FKPM).

In the EMM, electromagnetic fields from the coil set are calculated, including both inductively and capacitively coupled power. In this study, the applied RF voltage amplitude and phase (with respect to current) on the coil set are specified based on experimental measurements. The capacitively coupled power from the voltage on the coil set is then calculated in the FKPM. The results from the EMM are iterated with the FKPM. Based on the capacitively coupled power from the previous iteration in the FKPM, the inductively coupled power is adjusted in the EMM to maintain the specified total power deposited.

In the EETM, we consider two populations of electrons: the bulk electrons and the ion-induced secondary electrons (IISE). The IISEs are electrons emitted from the sapphire tube of the ICP source and metal chamber walls by ion-impact and are tracked using the electron Monte Carlo Simulation (eMCS), referred to as the “beam eMCS.” The IISEs are typically energetic as they are accelerated through the sheath into the bulk plasma. The trajectories of the IISEs are tracked for one iteration, and any IISEs that remain at the end of that iteration are included as initial conditions for the following iteration. When the energy of an IISE falls below 3.5 eV, it is removed from the beam eMCS, and the density is added to the continuity equation for electrons. The energy transport of bulk electrons can be tracked using two different methods: the electron energy equation and the eMCS for the bulk electrons, referred to as the “bulk eMCS.” In the electron energy equation, the electron temperature T_e is calculated by solving the electron energy conservation equation. Rate coefficients for electron-impact reactions are calculated by solving a two-term spherical harmonic expansion of Boltzmann’s equation for a range of E/N values which also produces average energy or T_e. This forms a look-up table of electron-impact rate coefficients for different T_e. In the bulk eMCS, a kinetic method is used to calculate the electron energy distribution in each cell. Using this energy distribution, the electron-impact rate coefficients are determined, and T_e is calculated as $\frac{2}{3}\langle E\rangle$, where $\langle E\rangle$ is the average energy of the distribution. When the bulk

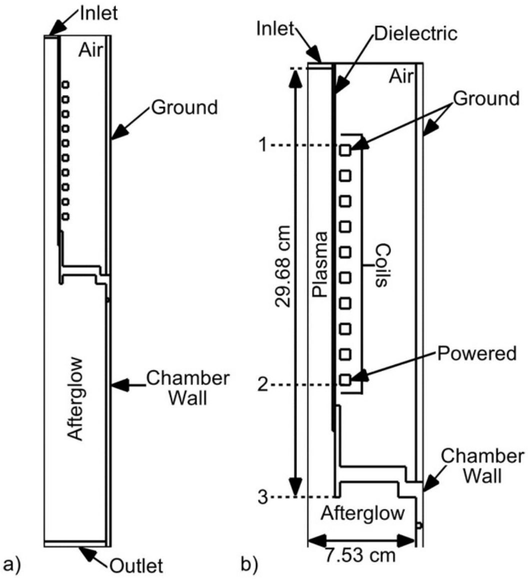

Figure 2. Geometry used in HPEM. (a) full chamber and (b) view zoomed in on the ICP. Dashed line 1 is the top of the coil set, dashed line 2 is the bottom of the coil set, and dashed line 3 is the ICP exit.

eMCS is used, stochastic heating is also included in the EMM using the currents calculated in the bulk eMCS. Note that in the eMCS, the electron trajectories are tracked in 3D, including electrostatic fields in r and z and electromagnetic fields in angle φ.

Fluid flow and chemical kinetics of the ions and neutral species are tracked in the FKPM. The continuity, momentum, and energy equations for each individual ion and neutral species are solved, as well as the continuity equation for electrons. Poisson's equation is also solved in this module as it is coupled to the continuity equations for the charged species. Since the electron momentum equation is not solved, the electron fluxes are calculated using the Scharfetter–Gummel formulation [27].

Initially, simulations considering only inductively coupled power, referred to as "pure ICP" simulations, were run. The pure ICP simulations use the electron energy equation to calculate T_e and were run for sufficient time for gas flow and gas temperature to reach a steady state. The cases are then restarted using the conditions for the neutral species at the end of the pure ICP simulations as initial conditions. The restarted cases use the bulk eMCS and include capacitively coupled power from the coil. This restart is simply a convenience to save computational time by having a more accurate initial condition. The restarted cases are referred to as ICP with capacitive coupling ("ICP with CC"). 30 000 particles are initially included in the bulk eMCS with a maximum of 300 000 particles that is reached early on in the simulation. The electron energy distribution functions (EEDFs) are averaged over successive calls to the bulk eMCS to improve the particle statistics, particularly in the spatial afterglow. Results presented in this study are at the conclusion of ICP with CC cases unless otherwise specified.

The cylindrically symmetric geometry of the Fiji G2 and diagnostics chamber used in the model is shown in figure 2. The mesh resolution is 0.175 cm radially and 0.353 cm axially, and the total dimensions of the mesh are 8.06 cm radially and 61.85 cm axially. The inner radius of the sapphire tube is 1.75 cm, matching the Fiji G2 source. The coil turns are separated by 1.06 cm and are placed 0.35 cm away from the 0.18 cm thick sapphire tube. In figure 2(b), dashed line 1 is located at the top of the coil set, while dashed line 2 is at the bottom of the coil set. The geometry near the exit of the ICP is shown in figure 2(b), matching the geometry in the experiments. The exit of the ICP, where the gas flows into the processing chamber, is represented by dashed line 3. The chamber is 31.11 cm long with a 7.53 cm radius. Gas flows out the bottom boundary with the pressure being held constant at the outflow boundary by adjusting the flow rate. The chamber walls and bottom boundary are both modeled as grounded metals. IISEs are emitted from the sapphire tube and chamber walls with an energy of 4 eV and an assumed secondary emission coefficient of $\gamma = 0.15$, in line with values used in other studies [25, 26]. The applied RF voltage is measured at the powered end of the coil nearest the ICP exit, while the current is measured on the ground side of the coil. In the model, the voltage amplitude is specified on powered end of the coil and assumed to linearly decrease to 0 V at the grounded end of the coil, while the phase with respect to current is held constant. In this study, the pressure is 10 mTorr or 100 mTorr, and the total power deposition varies from 50 W to 300 W.

10 Ar species are included in the model in addition to electrons: Ar, Ar(4s$[3/2]_2$), Ar(4s$[3/2]_1$), Ar(4s$[1/2]_0$), Ar(4s$[1/2]_1$), Ar(4p), Ar(4d), Ar_2^*, Ar^+, and Ar_2^+. 166 reactions occur between these species. Cross-sections for electron-impact reactions are taken from the LXCat database Magboltz 8.97 [28]. Penning reactions between Ar excited states can produce an electron, such as

$$Ar^* + Ar^* \rightarrow Ar^+ + Ar + e \quad \left(k = 1.2\times10^{-9}\left(\frac{T_{\text{gas}}}{298}\right)^{\frac{1}{2}} \text{cm}^3\text{s}^{-1}\right),$$

$$Ar^* + Ar^* \rightarrow Ar_2{}^+ + e \quad \left(k = 5.7\times10^{-10}\left(\frac{T_{\text{gas}}}{298}\right)^{\frac{1}{2}} \text{cm}^3\text{s}^{-1}\right).$$

These reactions occur between all combinations of electronically excited states of Ar. The electron produced in these reactions has an energy determined by the difference between the excitation energies of the reactants and the ionization potential of the product. For example, for Ar(4s$[3/2]_2$) + Ar(4s$[3/2]_2$) → Ar^+ + Ar + e, the electron carries away 7.3 eV of excess energy. This excess electron energy is included in the calculation of T_e for bulk electrons as a power source. In the pure ICP simulations, the excess electron energy is included in the electron energy equation, while for the ICP with CC cases, the energy is included in the bulk eMCS. The algorithm for including these electrons in the bulk eMCS is as follows. First, the number of electrons created from each reaction k $N_{\text{i,j,k}}$ is calculated by

$$N_{i,j,k} = R_{i,j,k}\, V_{i,j}\Delta t.$$

Here, i and j refer to the cell number in r and z, respectively. $R_{i,j,k}$ is the reaction rate in cm^{-3} s^{-1} of reaction k based on the previous iteration, $V_{i,j}$ is the volume of the cell, and Δt is the time between launching particles. Only reactions k that produce electrons, do not have an electron as a reactant, and have a specified excess electron energy are included. The total number of particles launched in the plasma N_{p} is calculated by

$$N_{\text{p}} = \frac{\sum_m W_m}{W_{\text{launch}}} \frac{\sum_{i,j,k} N_{i,j,k}}{\sum_{i,j} n_{e;i,j} V_{i,j}},$$

where W_m is the weight of particle m, W_{launch} is the weight of the particles to be launched (in this case, 1), and $n_{e;i,j}$ is the electron density at cell i,j. N_{p} particles are placed statistically according to the source function, and the velocity of each particle is randomly distributed with a total energy equal to the excess electron energy. The reaction Ar(4d) + Ar → $Ar_2{}^+$ + e also occurs, as Ar(4d) has a large enough excitation energy to make this reaction energetically favorable [29]. However, the electron produced has very little energy, and so the excess electron energy is not considered in the eMCS or electron energy equation. No other Ar excited states included in this study have enough energy to react with ground state Ar and produce an electron.

Two Ar excited states radiatively decay to the ground state: Ar(4s$[3/2]_1$) and Ar(4s$[1/2]_1$). However, these radiative transitions are trapped, as the emitted photon is re-absorbed by a ground state Ar to recreate the excited state that the photon was originally emitted from. To account for radiation trapping, the Einstein A coefficients A_{ji} are multiplied by the escape factor η_{ji} as used in Dwivedi and Hara [30]

$$\eta_{ji} = \frac{2 - \exp\left(-k_{ji}R/1000\right)}{1 + k_{ji}R},$$

$$k_{ji} = \frac{\lambda_{ji}^3 n_i}{8\pi}\frac{g_j}{g_i}A_{ji}\sqrt{\frac{m_{Ar}}{2\pi k_{\text{B}} T_{\text{gas}}}}.$$

Here, R is a characteristic length scale (in this case, the tube radius of 1.75 cm), n_{i} is the density of the absorbing state, m_{Ar} is the mass of Ar, k_{B} is Boltzmann's constant, and T_{gas} is the gas temperature (assumed to be 300 K). λ_{ji} is the wavelength of the transition, A_{ji} is the Einstein A coefficient, g_{j} is the degeneracy of the upper state, and g_{I} is the degeneracy of the lower state. The degeneracies are calculated by $2J + 1$, where J is the total angular momentum of the state. For Ar, $g_{\text{j}} = 3$ for both radiating states and $g_{\text{i}} = 1$ for the ground state. As the escape factor depends on the density of the ground state, the escape factors are different for 10 mTorr and 100 mTorr. The trapped rates are shown in table 1. Other radiative reactions included in the reaction mechanism involve Ar(4p) and Ar(4d) radiatively

Table 1. Trapped rates for radiative transitions.

Transition	Einstein A coefficient (s^{-1})	Trapped rate at 10 mTorr (s^{-1})	Trapped rate at 100 mTorr (s^{-1})
$Ar(4s[3/2]_1) \rightarrow Ar$	1.2×10^8	2.42×10^6	3.28×10^5
$Ar(4s[1/2]_1) \rightarrow Ar$	5.3×10^8	2.94×10^6	4.65×10^5

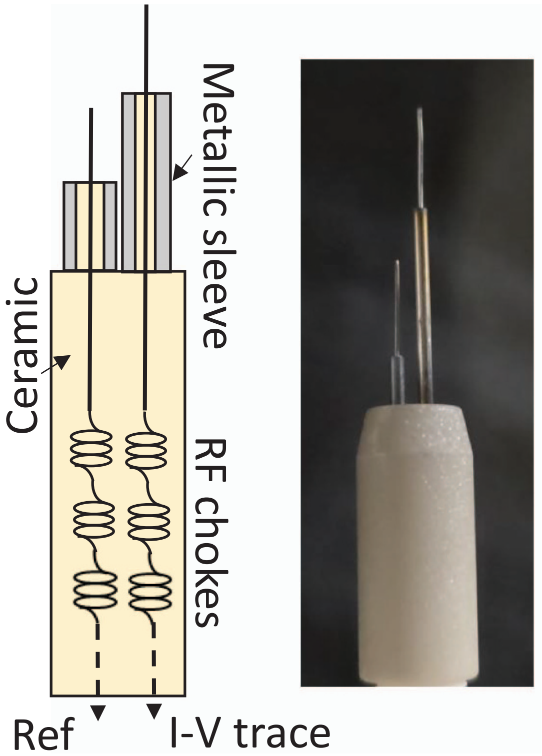

Figure 3. Schematic and photograph of the Langmuir probe used.

decaying to the Ar(4s) states. However, since the densities of the Ar(4s) states are much lower than that of the ground state, radiation trapping is not considered in these transitions. As photons are not tracked in this study, photon reactions in the gas phase or on surfaces are not included. In a pure Ar plasma, the exclusion of photon reactions is not expected to significantly change the results as the energetic photons produced in radiative transitions are trapped and cannot ionize the background Ar. However, with a molecular gas, the photons emitted from $Ar(4s[3/2]_1)$ and $Ar(4s[1/2]_1)$ would be able to excite or dissociate the molecular gas. In that case, tracking the photons may become important.

2.2. Experimental measurements

A Langmuir probe from Impedans Ltd was used to perform measurements of the plasma in the spatial afterglow of the ICP, as shown in figure 3. The Langmuir probe was constructed from tantalum (Ta) wire that is 0.04 cm in diameter and 1 cm long. A secondary reference probe tip, of similar dimensions to the measurement probe, is located 1 cm behind and offset by 5 mm from the measurement probe. The reference probe serves to compensate for the effect of low frequency plasma potential changes induced by the electron current collection at the measurement probe. The RF filtering electronics behind the measurement probe tip are housed in a dielectric tube, which is 0.635 cm in diameter. The Langmuir probe was mounted on a sliding linear motion vacuum feedthrough to enable measurements at different distances from the ICP exit, defined as the position where the gas flows into the diagnostics reactor as in figure 2(b). We note that the probe itself is too large to insert into the ICP without significant perturbation of the plasma, and so measurements were not made directly in the ICP tube.

The I–V curves obtained from the Langmuir probe can be analyzed to determine different plasma properties, including the electron density n_e and plasma potential V_p. Due to the RF filtering of the signal, the calculated value of V_p represents the time-averaged value of V_p over the RF cycle [31]. n_e is obtained from the probe current at the plasma potential. The EEDFs in m^{-3} $eV^{-3/2}$ are also obtained by the Langmuir probe. To convert to $\mathrm{eV}^{-3/2}$, the EEDFs are divided by n_e derived from integration the EEDF. From the EEDF, T_e is calculated as $\frac{2}{3}\langle E\rangle$, where $\langle E\rangle$ is the average energy of the distribution. The error bars associated with each parameter, determined using the variation in the I–V curves over 100 traces, is on the order of the data point size. They have been omitted for clarity.

Low energy electrons are not measured as efficiently as high energy electrons, leading to a depletion of low energy electrons in the measured EEDF. This depletion could be due to the presence of RF field gradients between the measurement and reference probe [31] or a change in the plasma resistance between the measurement and reference probe [32]. These effects are discussed in detail in section 3.2. To correct for these measurement uncertainties at low electron energies, the EEDFs were extrapolated from 7 eV to 0 eV using the Maxwellian form e^{e/kT_e}. 7 eV was chosen as the starting point for the extrapolation because it is below the first excitation energy of Ar of 11.55 eV. The EEDFs and T_e with and without this correction applied are discussed in this study.

The amplitude of the voltage oscillation on the powered end of the coil was measured using a 1000:1 high voltage probe from Tektronix (Model 6015 high voltage probe). A Rogowski coil (Tektronix TRCP 0600 current transducer) was used to independently monitor current. Based on previous measurements in this system, the voltage oscillates 125° out of phase with the current and with little variation over operating conditions. While the phase difference may vary over the length of the coil, it was not accounted for in the modeling. Calculations indicate that the overall results of the model are not sensitive to the phase difference between the current and voltage along the coil. Previous measurements over the operating pressures in this work (10–100 mTorr) suggest the power coupling efficiency should be approximately 80%–90%, with decreasing efficiency as the pressure increases [19].

3. Base case analysis

We first consider the base case of the G2 remote ICP source operating in pure Ar flowing at 200 sccm. The total power deposited into the plasma is 300 W, and the pressure maintained at the outflow boundary is 100 mTorr. The measured amplitude of the voltage oscillation on the powered end of the coil is 1150 V. Using the measured amplitude, the results of HPEM predict that 102.2 W of power is capacitively coupled and 197.9 W of power is inductively coupled. In section 3.1, the plasma properties predicted by HPEM are analyzed in detail. In section 3.2, the results of HPEM are benchmarked against Langmuir probe measurements. In section 3.3, the role of capacitive power coupling is further discussed.

3.1. Plasma properties

Properties of the gas, such as the Ar density and average gas temperature T_gas, are shown in figure 4. There is a pressure drop across the system from the inlet to the outlet. Above the coil set, the Ar density is elevated at 5.0×10^{15} cm^{-3} while T_gas remains low at 325 K, leading to an increase in pressure to around 170 mTorr above the coil set. The pressure decreases as the gas flows through the coil set but remains elevated relative to the 100 mTorr maintained at the outflow boundary. Between the ends of the coil, the Ar density decreases to a minimum of 1.1×10^{15} cm^{-3}. T_gas is elevated to 1080 K by exothermic reactions occurring in the plasma and by charge-exchange heating. In the spatial afterglow, T_gas decreases to 330 K, and the Ar density increases to 3.0×10^{15} cm^{-3}, corresponding to a pressure of 100 mTorr.

Plasma properties, including the electron density n_e, plasma potential V_p, electron temperature T_e, total power deposition P_dep, inductively coupled power deposition P_ind, and capacitively coupled power deposition P_cap, are also shown in figure 4. The power is largely deposited between the ends of coil with a maximum value of 5.3 W cm^{-3}. Most of the power between the ends of the coil is inductively coupled, as P_ind is an order of magnitude higher than P_cap and reaches 5.2 W cm^{-3}. Due to the spatial profile of deposited power, the electrons reach their maximum density of 5.0×10^{12} cm^{-3} between the ends of the coil. In this region, T_e exhibits a maximum near the walls and a minimum along the centerline of the reactor. This saddle shape has been previously noted in ICPs when local electron heating dominates over nonlocal heating processes [33]. T_e reaches a maximum of 3.2 eV between the ends of the coil. V_p, time-averaged over the RF cycle, reaches 32 V between the ends of the coil. It is important to note that the sapphire walls of the ICP charge, leading to a non-zero wall potential that varies depending on operating conditions. Outside the ICP, the walls are grounded and thus do not charge. For simplicity, the value of V_p is reported with respect to ground for all locations in this work. Near the bottom end of the coil, P_cap is negative, indicating the current is out of phase with the electric fields for a large portion of the RF cycle.

While P_ind decreases rapidly below the bottom end of the coil, P_cap increases to a maximum of 0.5 W cm^{-3}. This increase in P_cap heats the electrons, increasing T_e to a maximum of 3.5 eV between

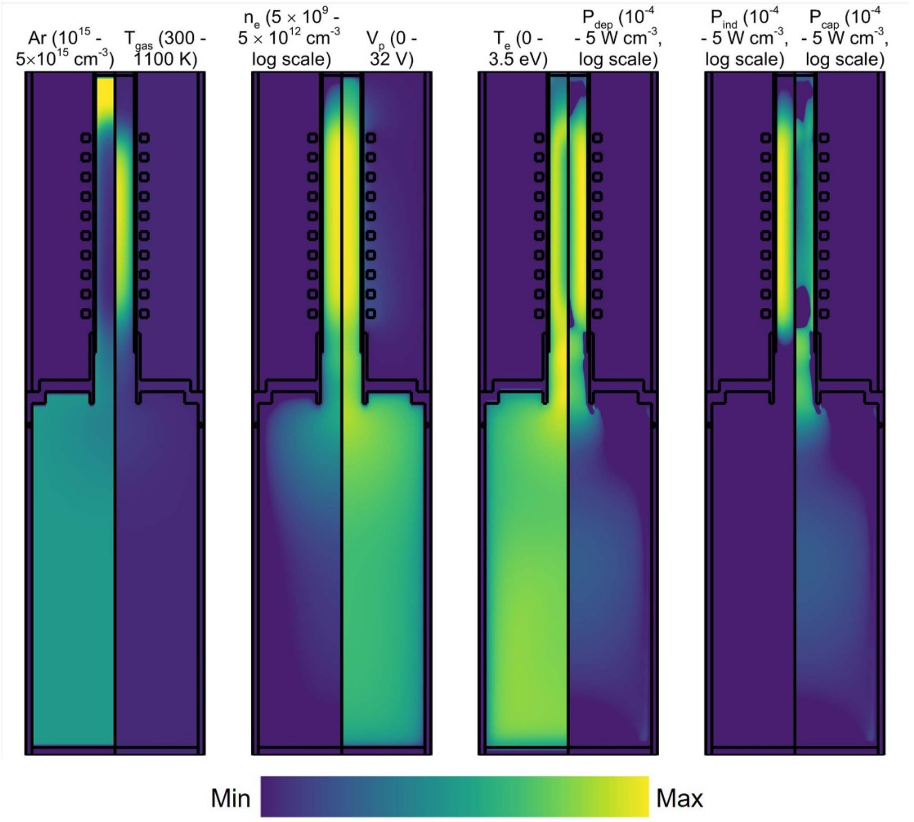

Figure 4. Plasma properties for operation at 200 sccm pure Ar at 100 mTorr and 300 W total power deposition.

the bottom end of the coil and the exit of the ICP. Despite P_{cap} heating the electrons, V_{p} and n_{e} decrease relative to their maximums between the ends of the coil as the overall power deposition P_{dep} decreases.

In the spatial afterglow, V_{p} decreases to approximately 20 V far from the ICP. Many of the electrons are confined in the ICP by the gradient in the plasma potential; however, energetic electrons can overcome the potential gradient to escape the ICP and enter the spatial afterglow. Electrons can also be produced in the afterglow by reactions between Ar excited states ($\mathrm{Ar}^* + \mathrm{Ar}^* \rightarrow \mathrm{Ar}^+ + \mathrm{Ar} + \mathrm{e}$ and $\mathrm{Ar}^* + \mathrm{Ar}^* \rightarrow \mathrm{Ar_2}^+ + \mathrm{e}$) and power leaking into the afterglow. However, n_{e} decreases in the afterglow as the downstream production of electrons does not offset the loss of electrons due to confinement by V_{p} and losses to the walls. T_{e} initially decreases outside the ICP, reaching a local minimum of 2.5 eV before increasing further in the afterglow to a local maximum of 2.9 eV. This increase in T_{e} in the afterglow is driven by a small amount of P_{dep} in the afterglow. This power is capacitively coupled from the electrostatic oscillating potential of the coil as shown by P_{cap}. While the power deposition is not enough to drive an electron avalanche in the afterglow (i.e. a large increase in the ionization rate), as evidenced by the continued decrease in n_{e}, the capacitive power deposition is enough to elevate n_{e} compared to what would be expected from free diffusion.

The densities of energetic species produced by the plasma are shown in figure 5 with the neutrals shown in figure 5(a) and the charged species shown in figure 5(b). The results of HPEM are extracted along the centerline and are plotted as a function of distance into the afterglow. 0 cm is the exit of the ICP as shown in figure 2(b) and shown by dashed line 3 in figure 5. Positive values of distance extend into the afterglow towards the outflow boundary, while negative values extend into the ICP towards the gas inlet. Dashed lines 1 and 2 represent the top and bottom of the coil set as shown in figure 2(b). The total density of Ar^* is highest inside the ICP where these excited states are produced by electron-impact excitation. The most abundant species are the Ar(4s) states with excitation energies ranging from 11.55 eV to 11.83 eV. The Ar(4p) and Ar(4d) lumped states have densities about two orders of magnitude lower than the $\mathrm{Ar(4s[3/2]_2)}$ metastable state. While most Ar excited states rapidly decay outside the ICP due to radiative processes, the two metastable states, $\mathrm{Ar(4s[3/2]_2)}$ and $\mathrm{Ar(4s[1/2]_0)}$, remain elevated in the afterglow as they do not radiatively decay to other Ar states. The metastable densities decrease by about an order of magnitude relative to their densities inside the ICP. The charged species

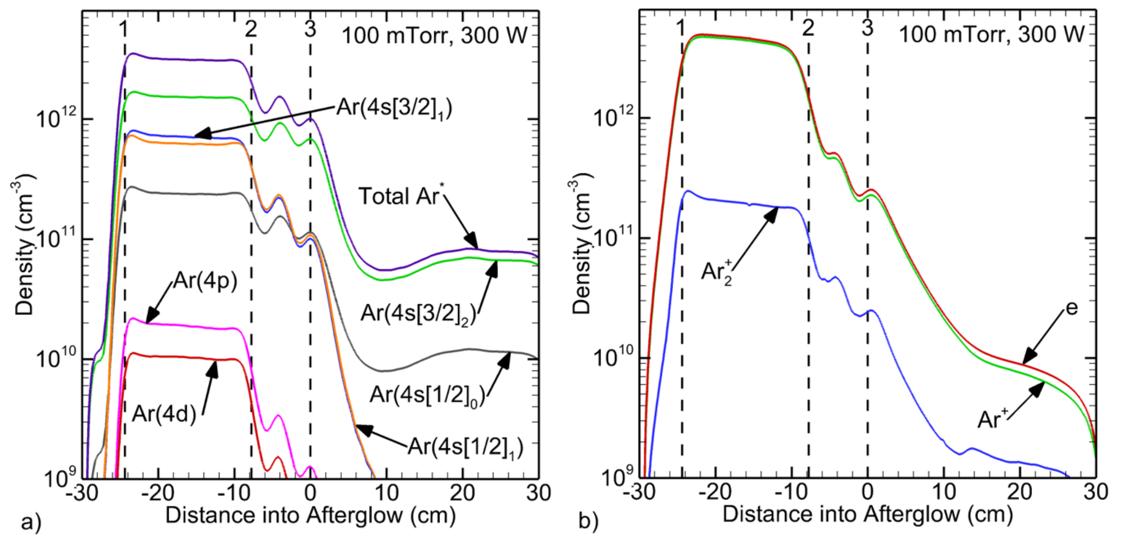

Figure 5. Densities of (a) neutral excited states and (b) charged species predicted by HPEM. Data is extracted along the centerline of the reactor ($r = 0$ cm). Dashed line 1 is the top of the coil set, dashed line 2 is the bottom of the coil set, and dashed line 3 is the ICP exit.

densities are shown in figure 5(b). The ion density n_i is highest inside the ICP and decreases into the afterglow, following the value of n_e. Inside the ICP, most of the ions are Ar^+, and the density of Ar_2^+ is over an order of magnitude lower than that of Ar^+. In the afterglow, both ion densities decrease at a similar rate. Comparing energetic neutrals with ions, the ion density exceeds the total excited state density by about a factor of 1.5 within the ICP. Outside the ICP, the ion density rapidly falls below the excited state density, and in the far afterglow, the excited state density can be at least an order of magnitude higher.

3.2. Comparison to Langmuir probe measurements

The results of HPEM discussed in section 3.1. are benchmarked against the experimental measurements in figure 6. n_e is shown in figure 6(a). Inside the ICP, n_e reaches a maximum of 4.9×10^{12} cm^{-3} at -22 cm and decreases towards the ICP exit. At the exit of the ICP, n_e as measured by the Langmuir probe is 1.1×10^{11} cm^{-3}, while the results of HPEM predict n_e of 2.5×10^{11} cm^{-3}. This is a reasonable match between the model results and experimental measurements. The results of HPEM show a small increase in n_e at 1 cm into the afterglow due to a local maximum in P_{cap} near the exit of the ICP. This small increase is not seen in the measurements. Beyond 1 cm, n_e decreases at a similar rate for the model results and measurements. The measurements show a plateau in n_e starting at 10 cm, while the model shows a plateau starting at 15 cm. At 15 cm into the afterglow, the results of HPEM predict an electron density of 1.1×10^{10} cm^{-3} that well matches the measurements of 1.2×10^{10} cm^{-3}.

V_p is shown in figure 6(b). Inside the ICP, V_p predicted by HPEM reaches a maximum of 32 V. V_p has a local maximum at -4 cm due to a local maximum in P_{cap}. At the ICP exit, V_p predicted by HPEM is 28 V, matching the measurements of 33 V within 5 V. As distance into the afterglow increases, V_p decreases in both the measurements and the results of the model. The rate of the decrease is similar between the measurements and the results of HPEM. The measurements show a plateau at 10 cm in V_p that is seen around 15 cm in the model results. At 15 cm, the model predicts the time-averaged V_p is 21 V, slightly underpredicting the measurement of 27 V.

The comparison of T_e is shown in figure 6(c). In this figure, the values of T_e with and without the Maxwellian correction of the probe derived EEDFs at low energies are shown. Above the top end of the coil at -25 cm, T_e increases to 3.1 eV. This local maximum drives the electron avalanche, as n_e increases rapidly above the top end of the coil. In the bulk plasma, T_e decreases to 2.2 eV. As n_e decreases below the bottom end of the coil, T_e once again increases due to a local maximum in P_{cap}. T_e as predicted by HPEM is 3.3 eV at the ICP exit, overpredicting the measurement of 2.1 eV by 1.2 eV. The measurements show that T_e increases in the afterglow starting at 1 cm. The measured T_e based on the original EEDF reaches 3.3 eV at 15 cm. With the Maxwellian correction, T_e decreases compared to the measurements without the correction beyond 5 cm, reaching 3.0 eV at 15 cm. The model predicts a decrease in T_e in the first 9 cm of the afterglow before showing an increase to 2.7 eV at 15 cm. While we are unaware of

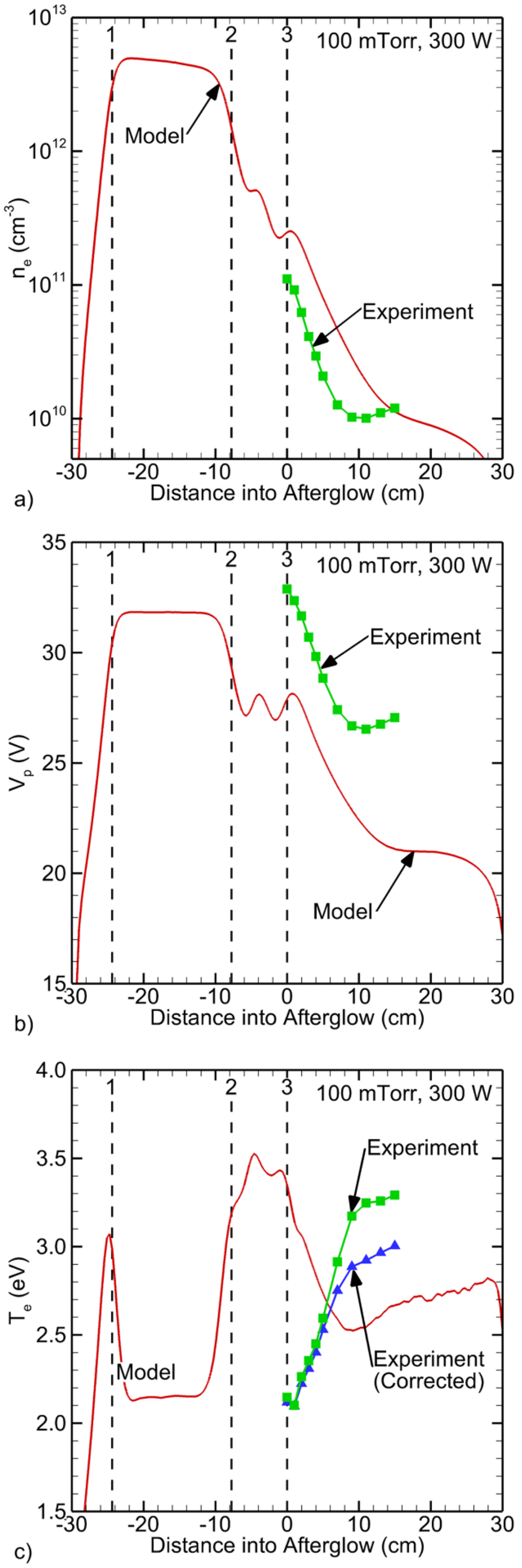

Figure 6. Comparison between model results and experimental measurements. (a) Electron density, (b) plasma potential, and (c) electron temperature. Data from HPEM is extracted along the centerline of the reactor ($r = 0$ cm). Dashed line 1 is the top of the coil set, dashed line 2 is the bottom of the coil set, and dashed line 3 is the ICP exit.

other reported measurements of T_e in remote ICP systems, Takao *et al* showed the region of high T_e extended further from the coil when capacitive coupling was included in a miniature ICP [34].

We can investigate the difference in T_e further by examining the EEDFs. The EEDFs with and without the Maxwellian correction at 0 cm, 5 cm, and 15 cm from the ICP exit are shown in figure 7. At the ICP exit (figure 7(a)), the Maxwellian correction does not significantly change the low energy

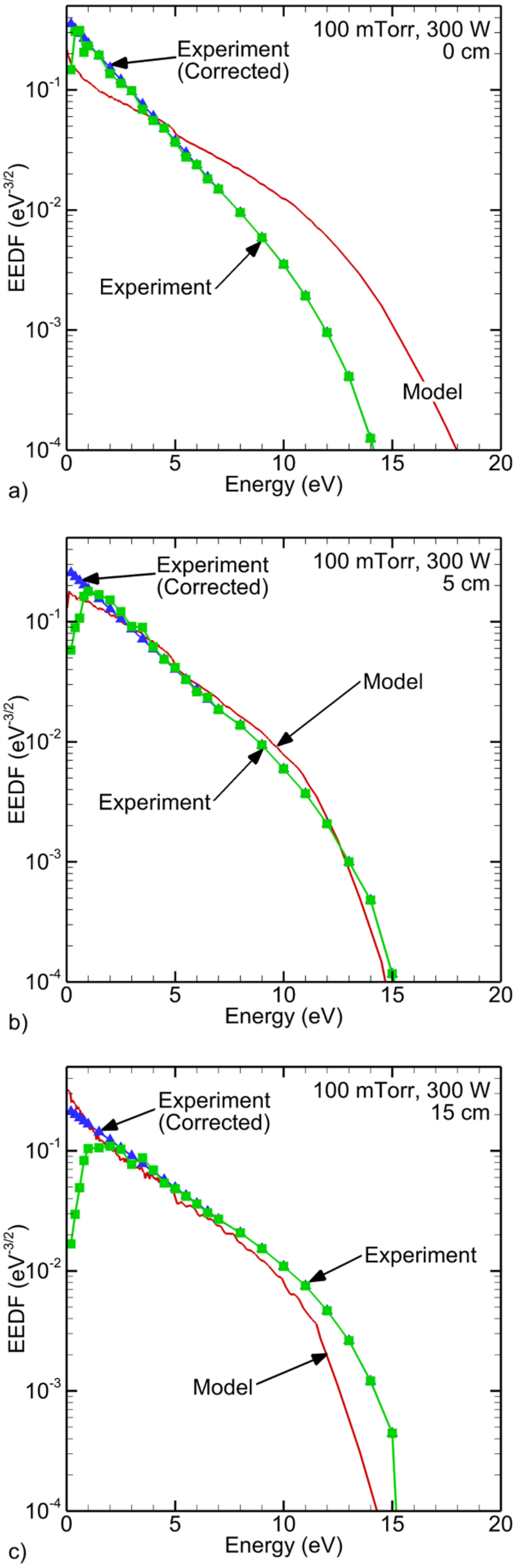

Figure 7. Comparison between model results and experimental measurements for the EEDFs. (a) 0 cm, (b) 5 cm, and (c) 15 cm from the ICP exit along the centerline.

portion of the EEDF. The measured EEDF shows a large population of electrons below 3.5 eV that is underpredicted by the model. Above 5 eV, the results of the model overpredict the measured EEDF. This underprediction of low energy electrons and overprediction of high energy electrons by the model leads to the higher T_e predicted by HPEM than measured at the ICP exit. At 5 cm, there is close agreement in the T_e predicted by HPEM (2.7 eV) and the corrected measurement (2.5 eV). Since there is close agreement in T_e, we expect close agreement in the EEDFs. The EEDF predicted by HPEM does indeed match the experimental measurements well. At 15 cm, the results of the model show a large population of electrons below 1 eV. The measurements without the correction show a depletion of these electrons. Despite the good agreement between the EEDFs above 2 eV, the discrepancy at low energies causes an underprediction of T_e without the correction by the model. However, the corrected EEDF does not have this depletion of low energy electrons and matches the modeled EEDF relatively well. As the corrected measurement of T_e and modeled T_e agree within 0.3 eV, the agreement in the EEDFs is expected.

Overall, the results of HPEM match the experimental measurements relatively well. Both the model and measurements show a decrease in n_e and V_p with increasing distance from the ICP exit. The trends in T_e are not as well matched, due largely to the differences in the low and high energy parts of the measured and modeled EEDF near the ICP exit. Importantly, the magnitudes of those plasma properties are matched reasonably well. Both the model results and measurements show n_e, V_p, and T_e do not monotonically decrease with increasing distance from the source, which is linked to the influence of capacitive power coupling in the afterglow.

There a few possible reasons for the differences between the model results and experimental measurements. First, the Langmuir probe measurements, particularly near the ICP exit, may be significantly disturbing the plasma. Near the ICP exit, the probe and its housing have a radius of 0.63 cm, a significant fraction of the ICP radius (1.75 cm). Therefore, the Langmuir probe may be collecting enough electrons to alter the plasma characteristics. Moreover, Langmuir probe measurements in RF environments are particularly susceptible to deviations in T_e and V_p due to the influence of the RF fields. While standard techniques [31, 35] involving RF chokes matched to the driving frequency harmonics (13.56 MHz, 27.1 MHz, 40 MHz, 54 MHz) were used to compensate for these effects, it is possible that strong RF field gradients may be present in this experimental configuration. These gradients could pose an additional source of error if they are significant over distances commensurate with the spacing between the Langmuir probe and its RF reference electrode [31]. Another potential source of error is associated with the finite plasma resistance between the measurement probe and reference probe in cases of high neutral pressure and low electron density as recently detailed by Andreev *et al* [32]. While the results detailed in [32] were performed at 1.5 Torr and in He, this effect could still be playing a role at 100 mTorr in Ar. Since this effect is more relevant at low electron density, we expect this effect to be more significant as distance into the afterglow increases, resulting in an under representation of low energy electrons in the uncorrected EEDFs shown in figures 7(b) and (c). When the Maxwellian correction is applied to account for the depletion of the low energy electrons, the measured EEDFs and T_e better match the modeled EEDFs and T_e as distance into the afterglow increases.

Another possible reason for the discrepancies between the model and experiment is that the power transfer efficiency in the experiments is expected to be approximately 80%–90% while the model assumes all of the power is deposited into the plasma. This overprediction would likely result in an increased P_{ind} compared to the experiment, changing the plasma properties inside the ICP source. This change would then impact the downstream plasma, including P_{cap}, n_e, V_p, and T_e, and could shift the location of the maximums of P_{cap} near the ICP exit, further impacting the plasma properties. The spatial afterglow geometry used in the model may also affect P_{cap}. In particular, increasing the distance to the outflow boundary may change P_{cap}, and in turn T_e, in the far afterglow. Another source of error unaccounted for in the modeling could be system drift over the course of making the voltage and current measurements on the coil and the downstream Langmuir probe measurements.

Although sensitive to the conditions, the experimental measurements show an increase in T_e deep into the afterglow where the electron density is decreasing. This indicates that the average electron is being heated at a higher rate than energy dissipation by collisions. Penning processes can provide such a heating source, but the magnitude of this heating source is too small to account for the significant increase in T_e. The remaining possible heating source is electrostatic capacitive coupling, which produces both bulk Joule heating and sheath associated stochastic heating. The magnitude of this capacitive heating is sensitive to the geometrical details of the chamber and the material properties in contact with the plasma (i.e. permittivity, conductivity).

3.3. Role of capacitive power coupling

With the benchmarked results of HPEM, we further examine the role of capacitive power coupling in the afterglow. Power coupling influences the production of electrons and ions through electron-impact ionization. The net source functions of electrons due to reactions with bulk electrons, IISEs, and neutrals are shown in figure 8 as a function of distance into the afterglow. Between the ends of the coil, most of the electrons are produced in electron-impact reactions with bulk electrons as n_e is high with a reasonably high T_e. The rate for electron production by bulk electrons in the center of the ICP source is

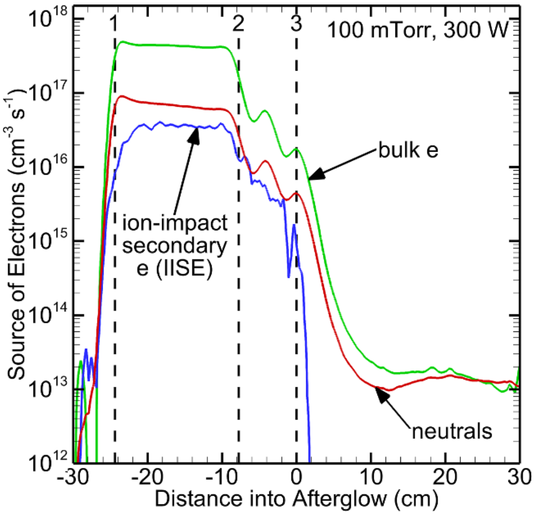

Figure 8. Source of electrons due to bulk electrons, ion-impact secondary electrons (IISE), and neutrals. Data from HPEM is extracted along the centerline of the reactor ($r = 0$ cm). Dashed line 1 is the top of the coil set, dashed line 2 is the bottom of the coil set, and dashed line 3 is the ICP exit.

4.3×10^{17} cm^{-3} s^{-1}. The contribution of reactions involving only neutral reactants to electron production (i.e., $Ar^* + Ar^* \rightarrow Ar^+ + Ar + e$, $Ar^* + Ar^* \rightarrow Ar_2{}^+ + e$) is nearly an order of magnitude lower, with a rate of 6.8×10^{16} cm^{-3} s^{-1} in the center of the ICP source. This source is driven primarily by $Ar(4d) + Ar \rightarrow Ar_2{}^+ + e$, as there is abundant Ar to react with Ar(4d). The production of electrons from IISEs is lower still with a rate of approximately 3.6×10^{16} cm^{-3} s^{-1}.

Below the bottom end of the coil, the rates all decrease relative to those inside the ICP source. A local maximum is seen in the production from bulk electrons and neutrals as P_{cap} reaches a maximum below the bottom end of the coil. In the spatial afterglow, the production of electrons from IISEs rapidly decreases. This decrease occurs as both the distance to the wall increases and n_i decreases, leading to less IISEs being produced in the afterglow. The production of electrons from bulk electrons decreases rapidly, following n_e. However, there is still a net production of electrons from bulk electrons in the afterglow, driven by the elevated P_{cap} and T_e. The production from neutrals decreases less rapidly, as the metastable states of Ar have a relatively long lifetime and flow downstream with the gas flow. The neutral reactions producing electrons in the afterglow include reactions between Ar metastable states, as well as $Ar(4d) + Ar$. In fact, at 25 cm into the afterglow where a substrate could be placed, the production of electrons from bulk electrons and from neutrals is about the same at 1.3×10^{13} cm^{-3} s^{-1}.

We can examine how the plasma properties change when there is no capacitive power coupling. The differences between the plasma properties in the pure ICP simulation and ICP with CC simulation are shown in figure 9. As discussed in section 2.1 capacitive power coupling is not considered in the pure ICP simulation, and the total power of 300 W is only inductively coupled. The electron energy equation is used to calculate T_e instead of the eMCS, and stochastic heating is not considered. Despite these differences, we compare these two cases to illustrate the effect of capacitive power coupling on the plasma in the afterglow. In the pure ICP simulation, P_{dep} is confined to the volume between the ends of the coil, resembling P_{icp} in figure 4. Accordingly, n_e is largely confined to the ICP source, decreasing below 10^9 cm^{-3} above the ICP exit. P_{dep} in the ICP with CC case includes capacitive coupling, which occurs primarily between the bottom end of the coil and the ICP exit, as well as a small amount in the afterglow. The plasma density is greater than the pure ICP case, and the capacitive power deposition elevates n_e below the bottom end of the coil and into the afterglow.

V_p is low in the pure ICP simulation compared to ICP with CC simulation. V_p in the pure ICP simulation reaches a maximum of 8 V with respect to ground inside the ICP and is 2 V at the ICP exit. V_p increases slightly in the afterglow, reaching a maximum of 5 V. In contrast, V_p in the ICP with CC simulation reaches 32 V inside the ICP and is 28 V at the ICP exit. T_e also differs between the pure ICP and ICP with CC cases. In the pure ICP simulation, T_e is higher between the ends of the coil than in the ICP with CC case and does not exhibit the saddle shape seen with capacitive coupling. In addition to the inclusion of capacitively coupled power, the bulk eMCS is used to calculate T_e instead of the electron energy equation. Therefore, it is expected that T_e, particularly inside the ICP where the power is largely deposited, would differ between these two simulations. In the afterglow, T_e decreases rapidly in

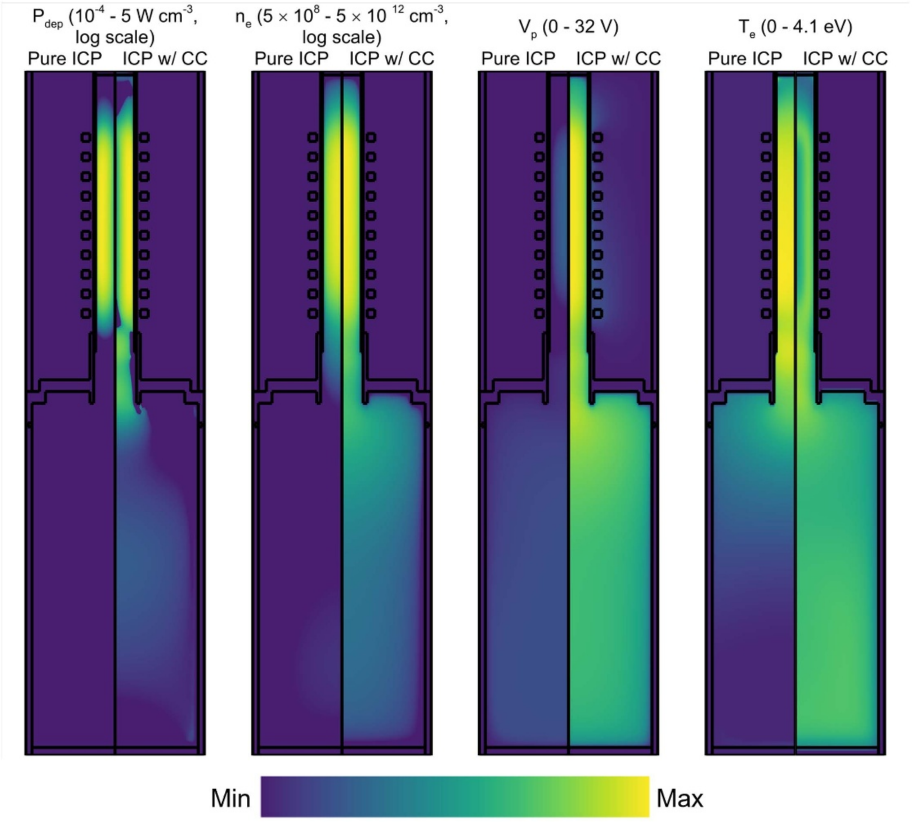

Figure 9. Comparison of total power deposition, electron density, plasma potential, and electron temperature between the pure ICP case (left) and ICP with capacitive coupling case (right). Operating conditions are 200 sccm pure Ar at 100 mTorr and 300 W total power deposition.

the pure ICP simulation and does not remain elevated as in the ICP with CC simulation. Therefore, the elevation of n_e, V_p, and T_e in the ICP with CC simulation is due to the small amount of P_{dep} that is capacitively coupled into the afterglow.

4. Influence of operating conditions

To fully benchmark HPEM against experimental measurements, we investigated a range of different process conditions. In this section, we compare the results of HPEM to experimental measurements for varying pressure (section 4.1) and power (section 4.2).

4.1. Pressure

The pressure of the system changes the collisionality of the plasma. As the pressure decreases, the neutral density decreases, decreasing the neutral collision frequency. We model the plasma at 10 mTorr to investigate a low collisionality operating condition compared to the base case of 100 mTorr. This pressure refers to the pressure maintained at the outflow boundary. The total power deposition is kept constant at 300 W.

The measured amplitudes of the voltage oscillation on the powered end of the coil at 10 mTorr and the base case of 100 mTorr are shown in table 2. The measured voltage amplitude is 1350 V for 10 mTorr and decreases to 1150 V at 100 mTorr. Based on the increased voltage amplitude at 10 mTorr, HPEM predicts a higher P_{cap} at 10 mTorr (139.1 W) than at 100 mTorr (102.2 W). For both pressures, power coupling is still primarily inductive.

The comparison between the model and experiments for 10 mTorr is shown in figure 10 and tables 3–5. The comparison for n_e is shown in figure 10(a). Similar to the results at 100 mTorr, n_e reaches a maximum near the top of the coil set of 1.9×10^{12} cm^{-3} at −21 cm. n_e then decreases towards the ICP exit, particularly below the bottom of the coil set. At the exit of the ICP, HPEM predicts an electron density of 2.3×10^{11} cm^{-3}, overpredicting the measurements of 4.8×10^{10} cm^{-3} by a factor of 4.6 as shown in table 3. This is a larger overprediction than the factor of 2.3 seen at 100 mTorr. Both the results of HPEM and measured n_e decrease further into the afterglow. The rate of decrease in

Table 2. Measured voltage amplitudes and model results for capacitively (P_{cap}) and inductively (P_{ind}) coupled power for varying pressure at 300 W total power deposition.

Pressure (mTorr)	Measured voltage amplitude (V)	Modeled P_{cap} (W)	Modeled P_{ind} (W)	P_{ind}/P_{cap}
10	1350	139.1	161.5	1.2
100	1150	102.2	197.9	1.9

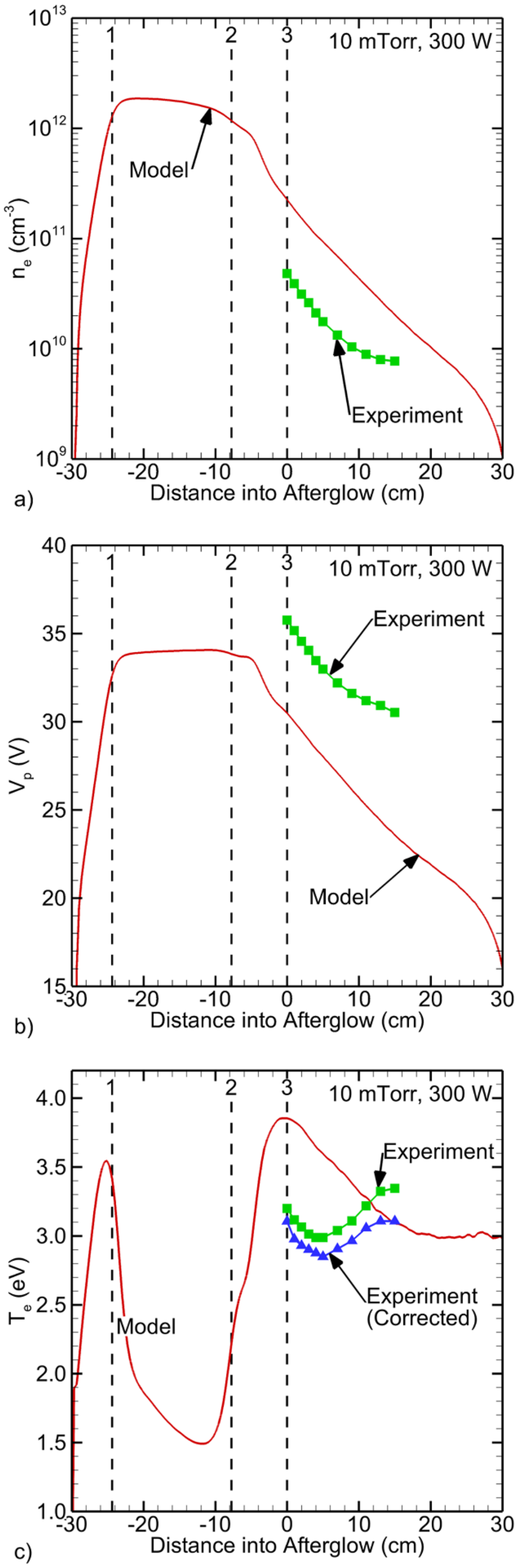

Figure 10. Comparison between model results and experimental measurements at 10 mTorr. (a) Electron density, (b) plasma potential, and (c) electron temperature. Data from HPEM is extracted along the centerline of the reactor ($r = 0$ cm). Dashed line 1 is the top of the coil set, dashed line 2 is the bottom of the coil set, and dashed line 3 is the ICP exit.

Table 3. Modeled and measured electron density for varying pressure at 300 W total power deposition.

Pressure (mTorr), position (cm)	Modeled n_e (cm^{-3})	Measured n_e (cm^{-3})	Modeled n_e /Measured n_e
10 mTorr, 0 cm	2.2×10^{11}	4.8×10^{10}	4.6
100 mTorr, 0 cm	2.5×10^{11}	1.1×10^{11}	2.3
10 mTorr, 15 cm	2.0×10^{10}	7.7×10^{9}	2.6
100 mTorr, 15 cm	1.1×10^{10}	1.2×10^{10}	0.9

Table 4. Modeled and measured plasma potential for varying pressure at 300 W total power deposition.

Pressure (mTorr), position (cm)	Modeled V_p (V)	Measured V_p (V)	Modeled V_p /measured V_p
10 mTorr, 0 cm	30.5	35.8	0.9
100 mTorr, 0 cm	27.9	32.9	0.8
10 mTorr, 15 cm	23.8	30.5	0.8
100 mTorr, 15 cm	21.1	27.1	0.8

Table 5. Modeled and measured electron temperature with the Maxwellian correction for varying pressure at 300 W total power deposition.

Pressure (mTorr), position (cm)	Modeled T_e (eV)	Measured T_e with Maxwellian correction (eV)	Modeled T_e /measured T_e
10 mTorr, 0 cm	3.9	3.1	1.3
100 mTorr, 0 cm	3.3	2.1	1.6
10 mTorr, 15 cm	3.1	3.1	1.0
100 mTorr, 15 cm	2.7	3.0	0.9

n_e between the model and experiments is similar to 9 cm. At 15 cm, n_e is measured as 7.7×10^9 cm^{-3} while HPEM predicts 2.0×10^{10} cm^{-3}, matching within a factor of 3.

The comparison for V_p is shown in figure 10(b). Inside the ICP, V_p reaches 34 V. This value is similar to the 32 V modeled in the 100 mTorr case, showing that V_p does not strongly depend on pressure. V_p decreases below the bottom end of the coil towards the ICP exit. At the ICP exit, the measured V_p is 35.8 V, while the V_p predicted by HPEM is 30.5 V, as shown in table 4. Outside the ICP, the rate of decrease of V_p predicted by HPEM matches the measurements well to 9 cm. At 15 cm, V_p predicted by HPEM is 23.8 V, matching the measurements of 30.5 V within 7 V.

The comparison for T_e is shown in figure 10(c). Similar to 100 mTorr, T_e increases above the top end of the coil, initiating the electron avalanche. T_e decreases inside the bulk plasma, reaching a minimum of 1.5 eV at −12 cm. T_e increases from −12 cm to the ICP exit at 0 cm as n_e decreases and as P_{cap} reaches a local maximum. At the ICP exit, the measured T_e with the Maxwellian correction is 3.1 eV while HPEM predicts 3.9 eV, as shown in table 5. This overprediction of 0.8 eV is smaller than the 1.2 eV overprediction at 100 mTorr. HPEM predicts a decrease in T_e until approximately 18 cm, where T_e plateaus at 3.0 eV. The corrected measurements show a decrease to 2.8 eV at 5 cm, followed by a slight increase to 3.1 eV at 15 cm. The corrected measurements are very similar to the measurements without the correction at this low pressure.

T_e can be further examined by investigating the EEDFs, shown in figure 11. At the ICP exit, the model well predicts the measured EEDF below 10 eV. The model overpredicts the high energy portion of the EEDF, particularly above 15 eV. This leads to the overprediction of the corrected T_e by 0.8 eV as shown in figure 10(c). The model continues to overpredict the high energy electrons at 5 cm from the ICP exit. At 15 cm from the ICP exit, the model results match the measured EEDF with the Maxwellian correction well as T_e matches.

The results of HPEM match the experimental measurements reasonably well at 10 mTorr. In particular, the magnitude of T_e is better matched at 10 mTorr than at 100 mTorr. The low energy portions of the EEDF without the Maxwellian correction are matched relatively well at all locations examined, indicating that the finite plasma resistance effect in the Langmuir probe measurements is not as relevant at 10 mTorr than at 100 mTorr. However, n_e is better matched at 100 mTorr than at 10 mTorr. This could

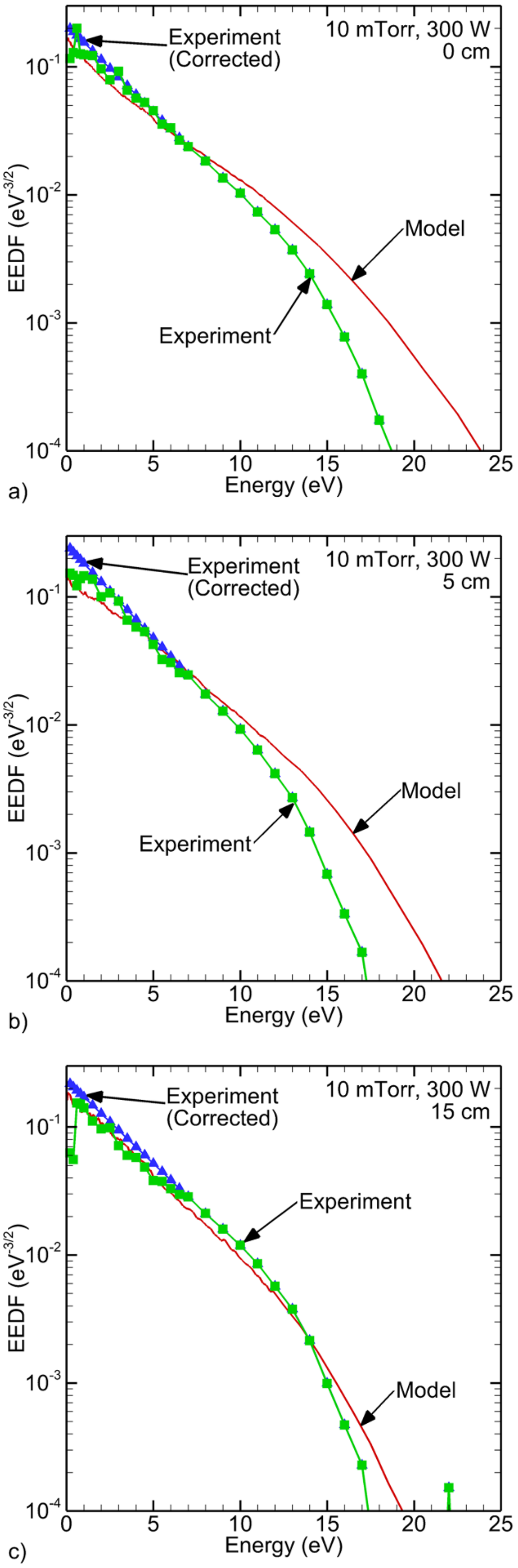

Figure 11. Comparison between model results and experimental measurements for the EEDFs at 10 mTorr. (a) 0 cm, (b) 5 cm, and (c) 15 cm from the ICP exit along the centerline.

be due to an overprediction of P_{cap} at the ICP exit or system drift, as discussed in section 3.2. Since the amplitude of the voltage oscillation is larger at 10 mTorr than at 100 mTorr, P_{cap} is larger and will more strongly affect the plasma properties near the ICP exit.

4.2. Power deposition

The total power deposited in the plasma directly changes n_e and the other plasma properties. When the total power deposition changes, the proportion of power that is inductively and capacitively coupled also changes. Since P_{ind} is primarily deposited between the ends of the coil and P_{cap} reaches a maximum near the ICP exit, changes in the mode of power deposition affect the plasma near the ICP exit. For this section, the pressure is kept constant at 100 mTorr at the outflow boundary.

The measured amplitudes of the voltage oscillation on the powered end of the coil are shown in table 6. In the low power cases (50 W and 100 W), the majority of the power is capacitively coupled. For 50 W, 72% of the total power (36.2 W) is capacitively coupled compared to only 28% (13.8 W) that is inductively coupled. However, in the high power cases (200 W and 300 W), most of the power is inductively coupled. These changes in coupling with increasing power indicate a mode transition between E-mode at low powers and H-mode at high powers.

The comparison between the model and experiments for varying powers is shown in figure 12. The comparison for 50 W is shown in the first column, 100 W in the second column, and 200 W in the third column. The comparison of n_e is shown in figures 12(a)–(c) for 50 W, 100 W, and 200 W. As expected, the maximum of n_e inside the ICP increases with increasing power. At 50 W, the maximum n_e occurs relatively close to the ICP exit at -11 cm. As power increases, the maximum shifts further into the ICP to -17.5 cm at 100 W and -22 cm at 200 W. The location of the maximum power deposition shifts further into the ICP as the relative contribution of P_{cap} decreases, leading to a shift in the position of the maximum n_e. At 100 W, there are two local maxima in n_e between the ends of the coil due to two local maximums in P_{ind}. Another local maximum in n_e occurs between the bottom end of the coil and the ICP exit at all three powers. This local maximum is due to an increase in P_{cap} near the ICP exit and is most prominent in the low power cases as a larger proportion of the power is capacitively coupled. The values of n_e are shown in table 7 at 0 cm and 15 cm into the afterglow for 50 W, 100 W, 200 W, and the base case of 300 W. At the ICP exit, the model overpredicts the measurements at 50 W by a factor of 6.5. This discrepancy decreases to a factor of 2.9 at 100 W. At 15 cm into the afterglow, the model still overpredicts the measurements by a factor of 7.9 at 50 W and a factor of 4.3 at 100 W. At 200 W, the model overpredicts the measurements by less than a factor of 2 at both the ICP exit and 15 cm into the afterglow, showing reasonable agreement. This is similar to 300 W, where the model overpredicts n_e at the ICP exit by a factor of 2.3 and matches within 10^9 cm^{-3} at 15 cm.

The comparison of V_p is shown in figures 12(d)–(f) for 50 W, 100 W, and 200 W. V_p inside the ICP does not strongly depend on the power deposition. The maximums in V_p inside the ICP roughly occur at the same position as the maximums in n_e, shifting as the maximum in power deposition shifts. The values of V_p at 0 cm and 15 cm into the afterglow are shown in table 8. V_p does not strongly depend on the power deposition at either location, with values within 6 V at each location. V_p matches the measurements within 7 V in all cases.

The comparison of T_e is shown in figures 12(g)–(i), for 50 W, 100 W, and 200 W. Inside the ICP, T_e reaches minimums when n_e reaches local maximums. In the low power cases, there is at least one local maximum in T_e between the ends of the coil. Since these cases are capacitively coupled, and n_e is not constant between the ends of the coil, T_e increases to drive the increase in n_e and exhibits at least one local maximum. At all powers, T_e reaches a maximum between the bottom end of the coil and the ICP exit due to a local maximum in P_{cap}. The values of T_e at the ICP exit and 15 cm into the afterglow are shown in table 9. At the ICP exit, the model overpredicts T_e by at least 1 eV at all powers. The model predicts a decrease in T_e until approximately 10 cm, after which T_e increases slightly. However, the measurements all show an increase in T_e from the ICP exit. At 15 cm in the low power cases, the measured T_e with the Maxwellian correction is at least 0.4 eV higher than the results of HPEM. However, in the high power cases, the corrected measurement of T_e agrees within 0.3 eV.

The EEDFs, shown in figure 13, can give insight into T_e. As power increases, the measured EEDF at the ICP exit shifts to lower energies as shown in figure 13(a)–(c). At all powers, the model underpredicts the low energy portion of the EEDF and overpredicts the high energy portion at the ICP exit. The discrepancies between the model and measurements increase as power increases, leading to the increased T_e discrepancy at this location as power increases. At 5 cm into the afterglow (figures 13(d)–(f)), there is relatively close agreement in the measured and modeled T_e in the low power cases. As expected, the EEDFs in the low power cases also match. At 200 W, the model overpredicts T_e by 0.6 eV at 5 cm. This overprediction is due to an underprediction of the low energy electrons as well as a slight overprediction in the high energy electrons, as shown in figures 13(f). At 15 cm (figure 13(g)–(i)), the measurements

Table 6. Measured voltage amplitudes and model results for capacitively (P_{cap}) and inductively (P_{ind}) coupled power for varying total power at 100 mTorr.

Power (W)	Measured voltage amplitude (V)	Modeled P_{cap} (W)	Modeled P_{ind} (W)	$P_{\mathrm{ind}}/P_{\mathrm{cap}}$
50	495	36.2	13.8	0.4
100	690	51.8	48.4	0.9
200	880	40.8	158.8	3.9
300	1150	102.2	197.9	1.9

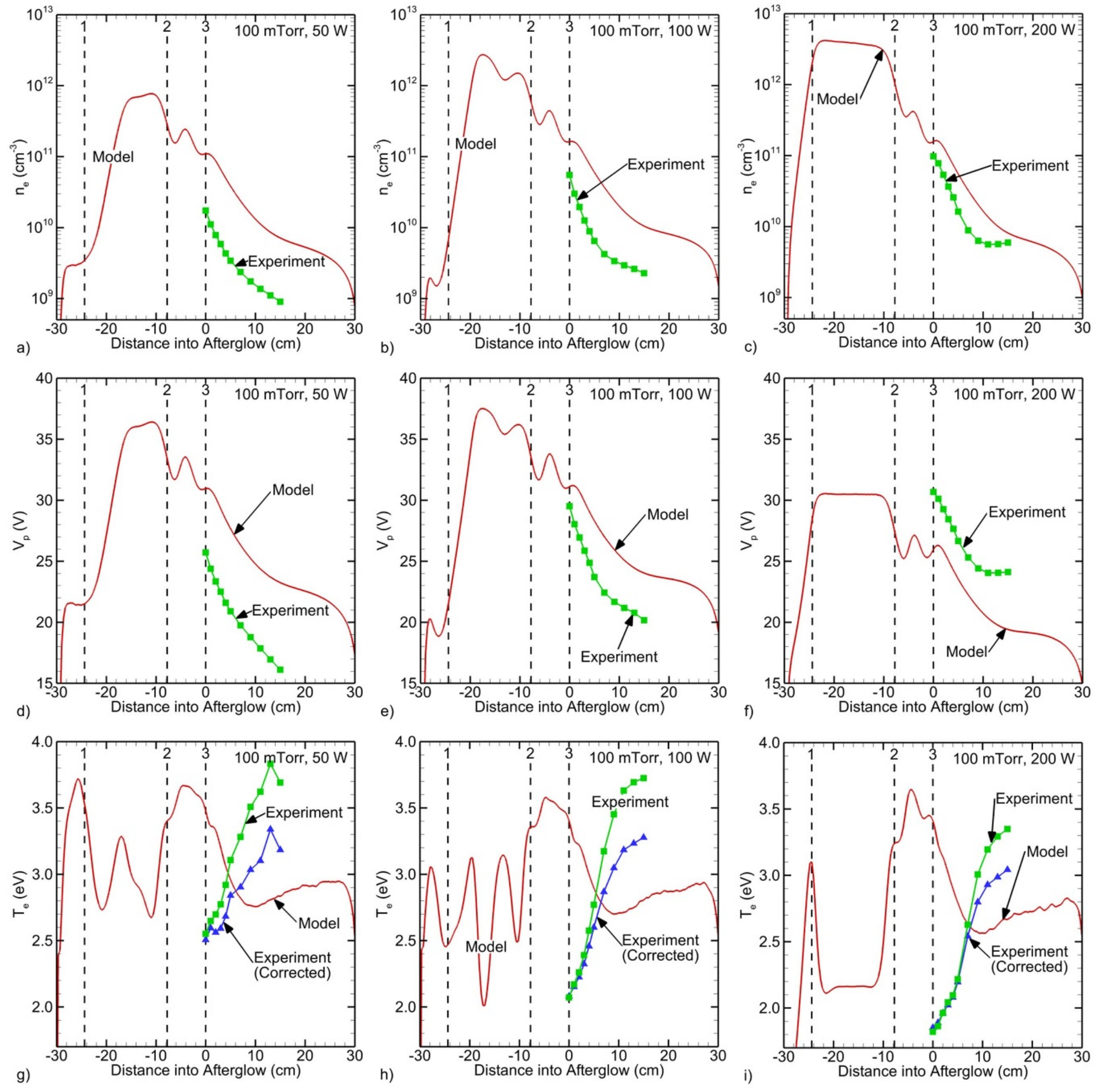

Figure 12. Comparison between model results and experimental measurements for varying total power. (a)–(c) electron density, (d)–(f) plasma potential, and (g)–(i) electron temperature. 50 W is shown in a, d, and g. 100 W is shown in b, e, and h. 200 W is shown in c, f, and i. Data from HPEM is extracted along the centerline of the reactor ($r = 0$ cm). Dashed line 1 is the top of the coil set, dashed line 2 is the bottom of the coil set, and dashed line 3 is the ICP exit.

show a higher T_e than predicted by HPEM at all powers. In the low power cases, the model underpredicts the high energy electrons in the EEDFs with the Maxwellian correction. At 200 W, the agreement in the high energy portion of the EEDF is good. While the EEDF as measured overpredicts the low energy electrons, the corrected EEDF matches the model results well.

In general, the low power cases have less agreement with the measurements than the high power cases, particularly in n_e. This discrepancy is likely due to the distribution of P_{cap} or system drift, as the power is mostly capacitively coupled in the low power cases. A difference in the location or magnitude of P_{cap} due to the increased power transfer efficiency in the model would have a larger impact on the low power cases compared to the high power cases. For the T_e comparison, the effect of the finite

Table 7. Modeled and measured electron density for varying total power at 100 mTorr.

Power (W), position (cm)	Modeled n_e (cm^{-3})	Measured n_e (cm^{-3})	Modeled n_e/measured n_e
50 W, 0 cm	1.1×10^{11}	1.7×10^{10}	6.5
100 W, 0 cm	1.6×10^{11}	5.5×10^{10}	2.9
200 W, 0 cm	1.6×10^{11}	9.7×10^{10}	1.6
300 W, 0 cm	2.5×10^{11}	1.1×10^{11}	2.3
50 W, 15 cm	7.1×10^{9}	9.0×10^{8}	7.9
100 W, 15 cm	1.0×10^{10}	2.3×10^{9}	4.3
200 W, 15 cm	8.1×10^{9}	5.9×10^{9}	1.4
300 W, 15 cm	1.1×10^{10}	1.2×10^{10}	0.9

Table 8. Modeled and measured plasma potential for varying total power at 100 mTorr.

Power (W), position (cm)	Modeled V_p (V)	Measured V_p (V)	Modeled V_p/measured V_p
50 W, 0 cm	31.0	25.7	1.2
100 W, 0 cm	31.1	29.5	1.1
200 W, 0 cm	26.0	30.7	0.8
300 W, 0 cm	27.9	32.9	0.8
50 W, 15 cm	23.2	16.1	1.4
100 W, 15 cm	24.0	20.2	1.2
200 W, 15 cm	19.4	24.1	0.8
300 W, 15 cm	21.1	27.1	0.8

Table 9. Modeled and measured electron temperature with the Maxwellian correction for varying total power at 100 mTorr.

Power (W), position (cm)	Modeled T_e (eV)	Measured T_e with Maxwellian correction (eV)	Modeled T_e/measured T_e
50 W, 0 cm	3.5	2.5	1.4
100 W, 0 cm	3.4	2.1	1.6
200 W, 0 cm	3.4	1.9	1.8
300 W, 0 cm	3.3	2.1	1.6
50 W, 15 cm	2.8	3.2	0.9
100 W, 15 cm	2.8	3.3	0.8
200 W, 15 cm	2.7	3.0	0.9
300 W, 15 cm	2.7	3.0	0.9

plasma resistance on the probe EEDFs could be influencing the changes in T_e as a function of position. As discussed in section 3.2, this effect will deplete the low energy electrons when n_e is low. We therefore expect this effect to increase T_e without the Maxwellian correction as n_e decreases and distance into the afterglow increases. At 15 cm into the afterglow (figure 13(g)–(i)), the measured EEDFs show a depletion of low energy electrons. This depletion is not present with the Maxwellian correction, and the agreement in the EEDFs at low energies is improved. However, the finite plasma resistance effect would have little effect on the measurement of high energy electrons that are underpredicted by the model at 50 W and 100 W [32].

5. Implications for ALD

The plasma properties, particularly in the spatial afterglow, are critical in determining the efficacy of PEALD systems that employ remote ICP sources. There are two goals when considering the energy flux delivered to the growth substrate during PEALD. The first is to provide enough energy to drive the requisite processes, and the second is to limit the energy flux to the substrate to minimize damage. In this section, we discuss the energy flux to the substrate through examining the plasma characteristics at 25 cm into the afterglow where a substrate would typically be placed. We also discuss strategies to decrease the energy flux to the surface, including the effect of operating conditions.

Both the ions and excited states can contribute to energy flux to the surface [4]. The energy flux density Γ_j for a given species j is

$$\Gamma j = f_j \cdot E_j = n_j \cdot v_j \cdot E_j,$$

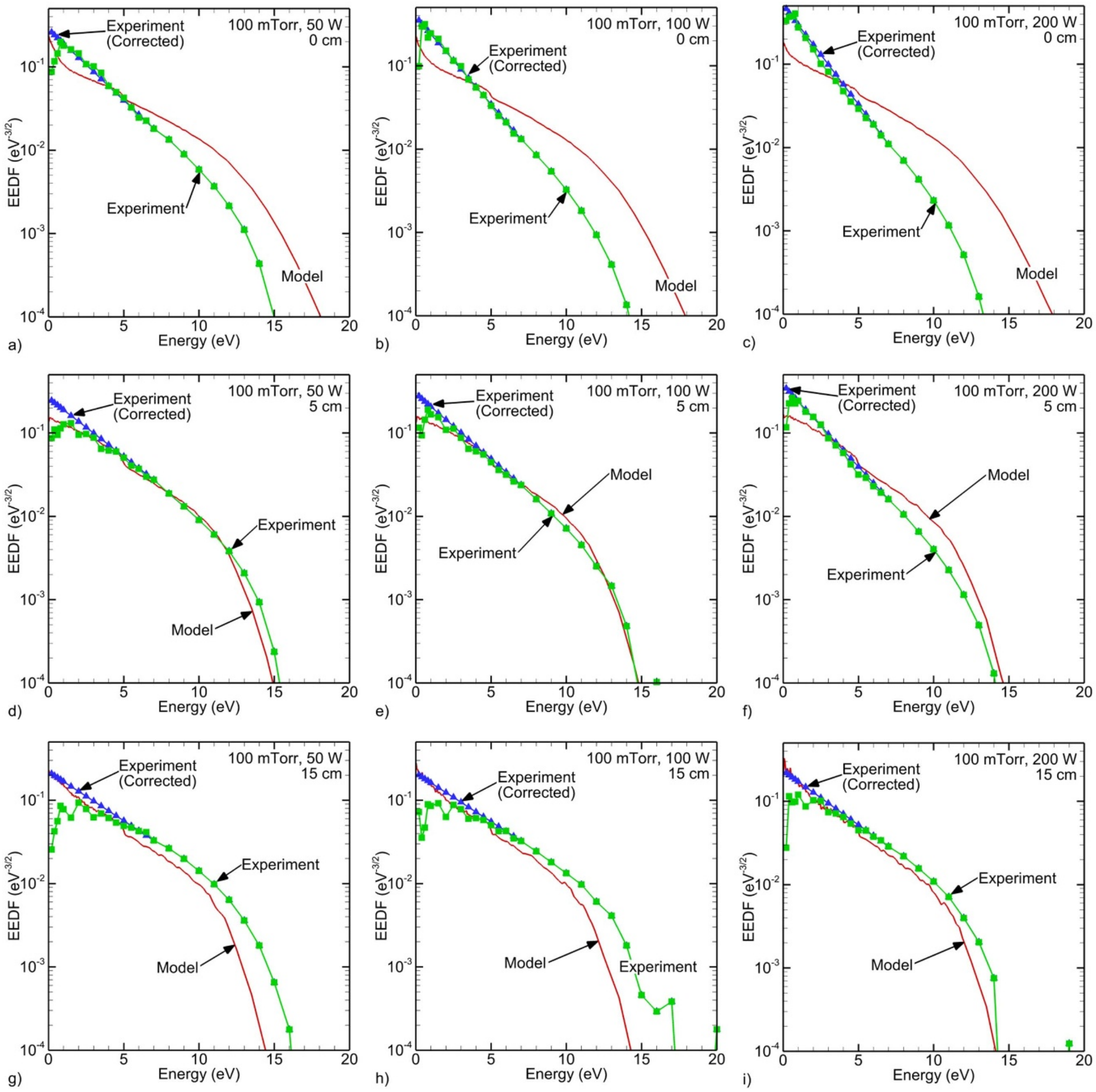

Figure 13. Comparison between model results and experimental measurements for the EEDFs. (a)–(c) 0 cm, (d)–(f) 5 cm, and (g)–(i) 15 cm. 50 W is shown in a, d, and g. 100 W is shown in b, e, and h. 200 W is shown in c, f, and i.

where f_j is the flux, n_j is the density, v_j is the velocity, and E_j is the energy delivered. The densities of energetic species produced by the plasma are shown in figure 5 as discussed in section 3.1 for the base case. In the spatial afterglow, the most abundant Ar excited states are the two metastable states, Ar(4s[3/2]$_2$) and Ar(4s[1/2]$_0$). At a typical substrate location 25 cm downstream of the ICP, the total Ar* density is 7.9×10^{10} cm^{-3}, due primarily to the Ar(4s[3/2]$_2$) metastable state. The Ar$^+$ density at 25 cm into the afterglow is 5.5×10^9 cm^{-3}, an order of magnitude lower than the Ar* density at that location. However, the velocity of ions and neutrals are different. The neutral thermal velocity is determined by the gas temperature, while the ion velocity before entering the sheath is determined by the Bohm velocity, which is in turn determined by T_e. To first order, the Bohm velocity will be greater than the neutral thermal velocity by an order of magnitude. Therefore, the flux of ions and excited neutrals into the sheath will be comparable at 25 cm into the afterglow.

The total energy delivered to the substrate by a given particle is comprised of both kinetic and potential energy. Most of the kinetic energy is imparted to the substrate by the ions as they are accelerated through the sheath that forms between the plasma and the substrate. The sheath voltage is on the order of V_p. Since the time-averaged V_p is 21 V at 25 cm into the afterglow in the base case, the ions will impact the substrate with an average energy of 21 eV. However, there is a distribution of ion energies, and the maximum ion energy will correspond to the maximum V_p. In the base case, the maximum V_p is 40 V at 25 cm into the afterglow. Therefore, the maximum energy an ion could have when impacting the substrate is 40 eV. Ar* states are not charged, and therefore, they are not accelerated by the sheath and impact the surface with a much lower kinetic energy (≈ 0.03 eV at 300 K). Of course, both Ar^+ and Ar^* have potential energy that can be transferred to the surface upon impact. Ar^+ can recombine with an electron and give energy to the surface determined by the difference between the ionization potential (15.82 eV) and work function for metals or electron affinity for semiconductors. Ar^* can be quenched on the surface, releasing the excitation energy of its specific excited state (at least 11.55 eV).

Most of the energy delivered to the surface by ions and excited states can be readily absorbed within a few nanometers of the surface [36]. The associated heating is therefore confined to the surface and can drive beneficial chemical and physical processes, including ALA. However, excessive energy delivery, particularly in the form of kinetic energy, can be problematic. If the kinetic energy exceeds the sputtering threshold of the substrate material, unwanted etching and/or defect generation can occur. Even with an energy below the sputtering threshold, defect generation is possible. To minimize the damage by ions to the substrate, the flux of ions with high kinetic energies should be reduced.

This reduction is readily achieved by reducing n_i and V_p near the substrate, with an emphasis on reducing V_p. As shown in section 3.3, the capacitively coupled power in the afterglow is responsible for the elevated V_p and n_e. Without any capacitively coupled power, V_p and n_e ($n_e \approx n_i$) are much lower in the afterglow, as shown in figure 9. We can more closely examine the plasma properties in the afterglow between the pure ICP and ICP with CC simulations, as shown in figure 14 along the centerline of the reactor. n_e, V_p, and T_e are all elevated in the ICP with CC simulation compared to the pure ICP simulation. n_e is decreased by approximately an order of magnitude at 25 cm into the afterglow in the pure ICP simulation compared to ICP with CC. In the pure ICP simulation, n_e begins increasing at 5 cm into the afterglow, driven by production of electrons from neutral reactions as production due to bulk electrons and IISEs decreases rapidly. T_e is also decreased in the pure ICP simulation, reaching a value of 0.1 eV, which is the minimum value allowed in the simulation. Both the time-averaged and maximum V_p are reduced in the pure ICP simulation. The time-averaged and maximum V_p are the same at 25 cm into the afterglow with a value of 5 V. However, in the ICP with CC simulation, the time-averaged V_p is 21 V and the maximum is 40 V. While the average ion energy is approximately the time-averaged V_p, the maximum ion energy corresponds to the maximum V_p. Depending on the material, ions with 40 eV of energy could sputter the substrate. The densities of $Ar(4s[3/2]_2)$ and Ar^+ are shown in figure 15 for the pure ICP simulation. The $Ar(4s[3/2]_2)$ density is 2.8×10^9 cm^{-3} at 25 cm into the afterglow, a factor of 24 lower than the 6.7×10^{10} cm^{-3} at the same location for ICP with CC. The Ar^+ density is 5.8×10^7 cm^{-3} at 25 cm into the afterglow, almost two orders of magnitude lower than the 5.5×10^9 cm^{-3} for ICP with CC. Since V_p and n_i are both lower in the afterglow, a system with only inductive power coupling will decrease the flux of energetic species to the substrate.

As discussed in section 4, operating conditions of the plasma affect the power coupling and plasma properties in the afterglow. As pressure affects the collisionality of the plasma, the downstream n_e and V_p are affected, as shown in figures 16(a) and (b). While n_e is lower inside the ICP at 10 mTorr than at 100 mTorr, the decrease in n_e is more gradual outside the ICP at 10 mTorr. In fact, n_e is larger at 10 mTorr between 4 cm and 22 cm into the afterglow. The time-averaged V_p is also larger at 10 mTorr up to 24 cm. If the substrate were placed at 20 cm from the ICP exit, we would expect a larger energy flux to the substrate at 10 mTorr based on the increased n_e and V_p. However, at 25 cm, we expect similar energy fluxes to the substrate at 10 mTorr and 100 mTorr, as V_p is within 1 V and n_e is within 1.5×10^9 cm^{-3} (22% difference).

Another factor influencing energy flux to the substrate with different pressures is collisions within the sheath. At low pressure, the sheath is essentially collisionless, and the ions reach the substrate with an energy approximately equal to the sheath voltage. As pressure increases, collisions in the sheath increase. There are two points worth noting here. First, collisions serve to reduce the average energy of ions reaching the substrate. Ions that have realized the full sheath voltage are likely still present, albeit in reduced quantities. Second, an ion that undergoes a charge-exchange collision will produce a fast neutral and a slow ion, leading to the delivery of two particles with substantial kinetic energy. The total energy delivered to the surface will be the same as if the ions did not undergo a collision, but the total energy of each particle is reduced. That reduction is potentially beneficial, particularly if the reduced energy is below the damage threshold.

While pressure affects the collisionality of the plasma, power directly impacts n_e and other plasma properties. V_p and n_e at 25 cm into the afterglow are shown as a function of power deposition in figure 17. As discussed in section 4.2, the low power cases (50 W and 100 W) have more than half of the power capacitively coupled, while the high power cases (200 W and 300 W) have mostly inductive power coupling. This mode transition between 100 W and 200 W is seen in figure 17, where n_e and V_p decrease as power increases from 100 W to 200 W. These results show that mostly inductive power coupling leads to a lower n_e and n_i, as well as V_p, at the substrate location.

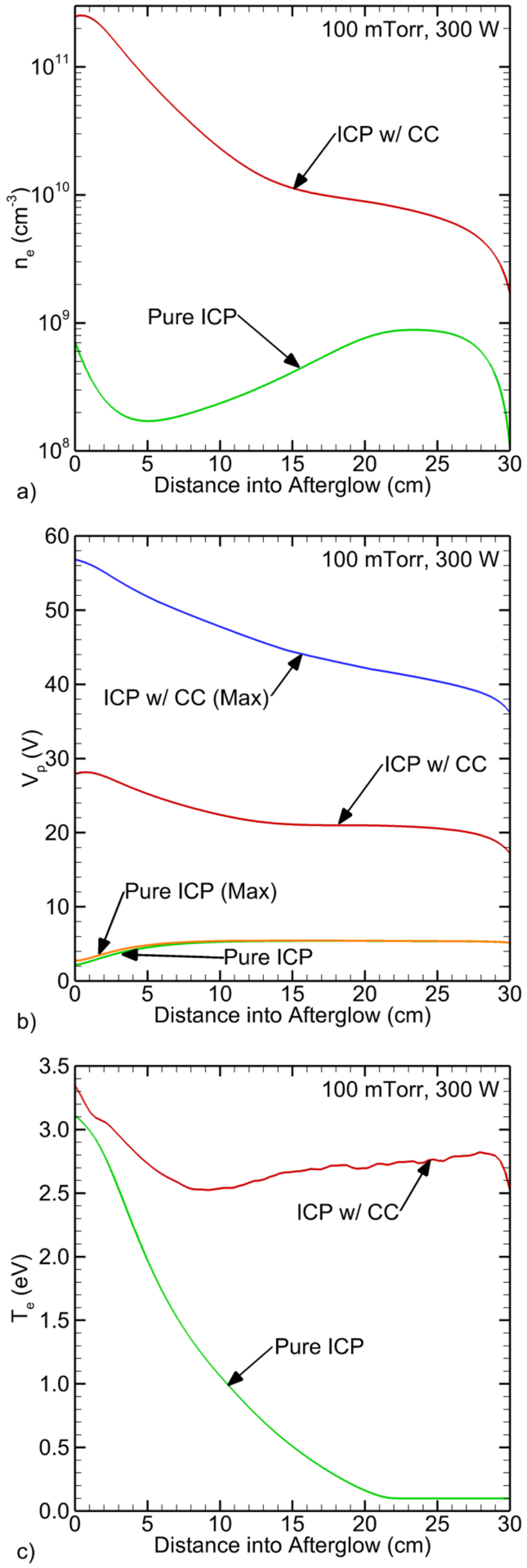

Figure 14. Comparison of plasma properties for the pure ICP case and ICP with capacitive coupling case. (a) Electron density, (b) plasma potential, and c) electron temperature. Data is extracted along the centerline of the reactor ($r = 0$ cm).

In addition to changing operating parameters, there are a few additional strategies to reduce the capacitive power coupling in this system, particularly in the afterglow. A different matchbox configuration could reduce the voltage on the coil and therefore the capacitive power coupling in both the ICP and in the afterglow. Another way to reduce the capacitive power coupling in the afterglow is to reverse the powered and grounded ends of the coil so the powered end of the coil is away from the ICP exit. In this configuration, most of the capacitive power coupling would likely be deposited between the ends of

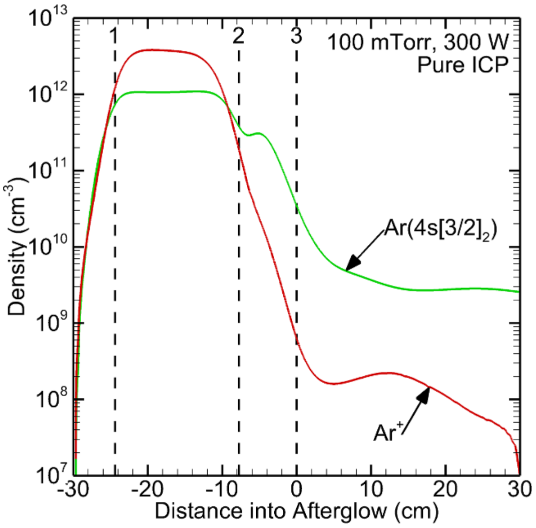

Figure 15. Densities of the Ar metastable state Ar(4s$[3/2]_2$) and Ar^+ predicted by HPEM for the pure ICP case. Data is extracted along the centerline of the reactor ($r = 0$ cm). Dashed line 1 is the top of the coil set, dashed line 2 is the bottom of the coil set, and dashed line 3 is the ICP exit.

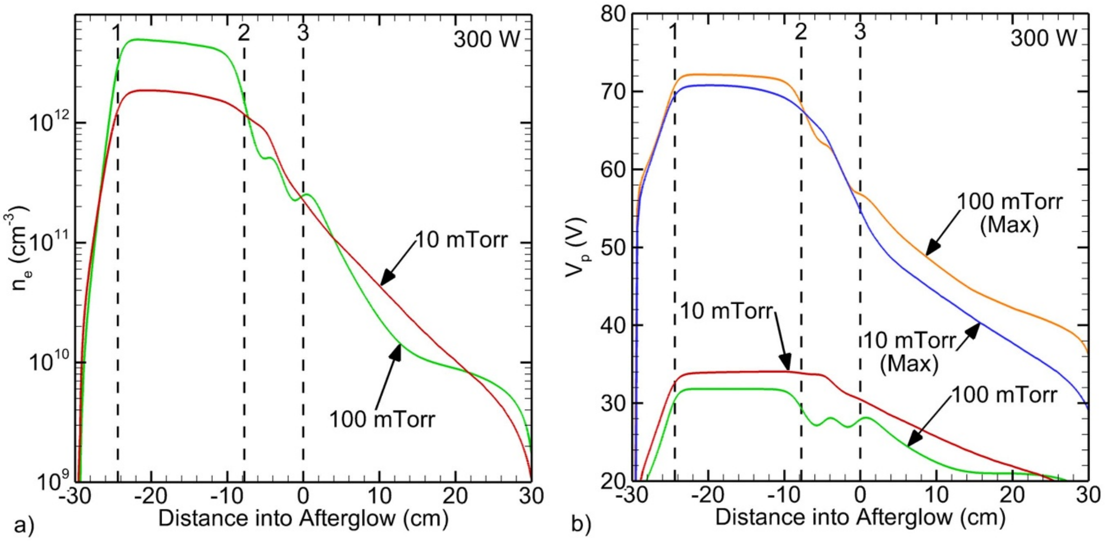

Figure 16. Plasma properties for 10 mTorr and 100 mTorr predicted by HPEM. (a) Electron density and (b) plasma potential. Data is extracted along the centerline of the reactor ($r = 0$ cm). Dashed line 1 is the top of the coil set, dashed line 2 is the bottom of the coil set, and dashed line 3 is the ICP exit.

the coil, lessening the power deposited below the bottom end of the coil and ICP exit as well as in the afterglow. Alternatively, a slotted Faraday shield could be incorporated into the ICP design to shield the electric fields generated around the coils and only allow inductive power coupling. While this approach would reduce the capacitive coupling effects, it would also significantly reduce the efficiency of power coupling between the antenna and plasma. Alternative antenna configurations proposed by Godyak and Alexandrovich could also reduce the capacitive coupling [37]. Finally, this study focuses on characterizing one particular ICP source commercially available for PEALD processing. However, changing the ICP source geometry would also affect the amount of capacitive power coupling. For example, increasing the radius of the ICP source at a constant power would decrease the volumetric power deposition, affecting the proportion of power that is inductively and capacitively coupled.

While pure Ar is not used except in ALA processes, the broader conclusions of this study are relevant for PEALD processes in all gas mixtures, including molecular gases. This work demonstrates that in

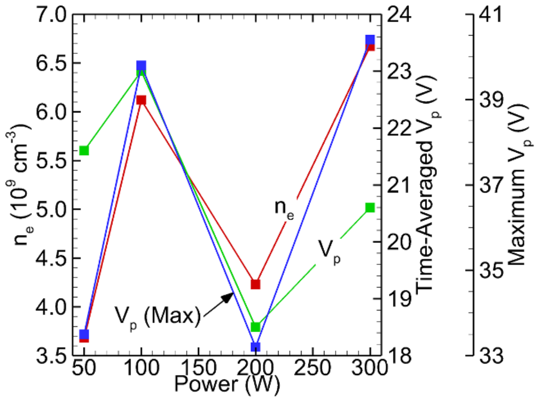

Figure 17. Electron density and plasma potential at 25 cm downstream of the ICP exit for varying power.

a remote ICP system, power is capacitively coupled into the afterglow, and that small amount of capacitively coupled power raises n_e and V_p in the afterglow. Previous work by Boris *et al* examined this system and a similar remote ICP system operating in Ar/N_2 mixtures [19]. They showed that n_e does not strongly depend on N_2 flow fraction, but V_p increases from 35 V at low N_2 fractions to 85 V at high N_2 fractions. They attributed the increase to downstream capacitive coupling.

6. Conclusions

In this study, we have modeled a commercially available ICP source for use in a remote PEALD geometry using the 2D model HPEM. We benchmarked the results of HPEM against experimental measurements in this system for different pressures and powers. Overall, the results of HPEM match the measurements reasonably well. The results of HPEM highlight the importance of capacitive power coupling in this system, particularly near the ICP exit into the processing chamber and in the spatial afterglow. The capacitive power coupling in the afterglow causes an increase in n_e, V_p, and T_e in the afterglow. While we examined the Veeco Fiji G2 remote ICP source, we expect capacitive power coupling will play a role in most helical remote ICP configurations.

From a PEALD perspective, decreasing capacitive power coupling reduces the energy flux to the surface by the ions and therefore provides a means to reduce ion-driven damage during growth. This damage reduction occurs as both n_i and V_p decrease with lower capacitive power coupling. The results show operating conditions affect the power coupling and lead to variations in n_i and V_p. Strategies for decreasing capacitive power coupling in this particular remote ICP system include changing matchbox configuration, placing the powered end of the coil far from the ICP exit, and using a Faraday shield or alternative antenna configurations. Alternatively, increasing the pressure can reduce the ion energy at the surface by increasing the collisionality of the sheath.

Acknowledgment

This work is supported by NRL base program funding. The simulations were completed in part using the Department of Defense’s High Performance Computing Modernization Program resources. M.E. Meyer appreciates the support of the National Research Council Postdoctoral Research Associateship Programs. The work of M. Kushner was supported by Samsung Electronics, Lam Research and Tokyo Electron America.

Data availability statement

All data that support the findings of this study are included within the article (and any supplementary files).

ORCID iDs

Mackenzie E Meyer 0000-0002-2105-6690
David R Boris 0000-0002-8382-4210
Michael J Johnson 0000-0002-9356-7772
Mark J Kushner 0000-0001-7437-8573
Scott G Walton 0000-0003-3893-3618

References

[1] Graves D B *et al* 2024 Science challenges and research opportunities for plasma applications in microelectronics *J. Vac. Sci. Technol. B* **42** 042202
[2] Oehrlein G S *et al* 2024 Future of plasma etching for microelectronics: challenges and opportunities *J. Vac. Sci. Technol. B* **42** 041501
[3] Arts K, Hamaguchi S, Ito T, Karahashi K, Knoops H C M, Mackus A J M and Kessels W M M 2022 Foundations of atomic-level plasma processing in nanoelectronics *Plasma Sources Sci. Technol.* **31** 103002
[4] Boris D R, Wheeler V D, Nepal N, Qadri S B, Walton S G and Eddy C R 2020 The role of plasma in plasma-enhanced atomic layer deposition of crystalline films *J. Vac. Sci. Technol. A* **38** 040801
[5] Knoops H C M, Faraz T, Arts K and Kessels W M M 2019 Status and prospects of plasma-assisted atomic layer deposition *J. Vac. Sci. Technol. A* **37** 030902
[6] Profijt H B, Potts S E, van de Sanden M C M and Kessels W M M 2011 Plasma-assisted atomic layer deposition: basics, opportunities, and challenges *J. Vac. Sci. Technol. A* **29** 050801
[7] Knoops H C M, Arts K, Buiter J W, Martini L M, Engeln R, Hemakumara D T, Powell M, Kessels W M M, Hodson C J and O'Mahony A 2021 Innovative remote plasma source for atomic layer deposition for GaN devices *J. Vac. Sci. Technol. A* **39** 062403
[8] Woodward J M *et al* 2022 Influence of plasma species on the early-stage growth kinetics of epitaxial InN grown by plasma-enhanced atomic layer deposition *J. Vac. Sci. Technol. A* **40** 062405
[9] Wheeler V D *et al* 2020 Phase control of crystalline Ga_2O_3 films by plasma-enhanced atomic layer deposition *Chem. Mater.* **32** 1140–52
[10] Faraz T, Arts K, Karwal S, Knoops H C M and Kessels W M M 2019 Energetic ions during plasma-enhanced atomic layer deposition and their role in tailoring material properties *Plasma Sources Sci. Technol.* **28** 024002
[11] Zhang Y, Ding Y and Christofides P D 2020 Multiscale computational fluid dynamics modeling and reactor design of plasma-enhanced atomic layer deposition *Comput. Chem. Eng.* **142** 107066
[12] Li H, Liu Y, Zhang Y-R, Gao F and Wang Y-N 2017 Nonlocal electron kinetics and spatial transport in radio-frequency two-chamber inductively coupled plasmas with argon discharges *J. Appl. Phys.* **121** 233302
[13] Tinck S and Bogaerts A 2011 Computer simulations of an oxygen inductively coupled plasma used for plasma-assisted atomic layer deposition *Plasma Sources Sci. Technol.* **20** 015008
[14] Gao F, Zhang Y-R, Li H, Liu Y and Wang Y-N 2017 Spatial distributions of plasma parameters in inductively coupled hydrogen discharges with an expansion region *Phys. Plasmas* **24** 073508
[15] Gao F, Li H, Yang W, Liu J, Zhang Y-R and Wang Y-N 2018 Experimental and numerical investigations of electron characteristics in 2 MHz and 13.56 MHz inductively coupled hydrogen plasmas with an expansion region *Phys. Plasmas* **25** 013515
[16] Jo S and Kim H J 2025 Reactor optimization strategies for remote plasma sources: numerical insights into argon inductively coupled plasma at Torr pressures *Phys. Fluids* **37** 013634
[17] Cheon C, Yoon J H, Jo S, Kim H J and Lee H J 2022 Importance of higher-level excited species in argon remote plasma sources: numerical modeling with consideration of detailed chemical reaction pathways *Plasma Process. Polym.* **19** e2100251
[18] Huang S, Volynets V, Hamilton J R, Lee S, Song I-C, Lu S, Tennyson J and Kushner M J 2017 Insights to scaling remote plasma sources sustained in NF_3 mixtures *J. Vac. Sci. Technol. A* **35** 031302
[19] Boris D R, Johnson M J, Woodward J M, Wheeler V D and Walton S G 2024 Remote inductively coupled plasmas in Ar/N_2 mixtures and implications for plasma enhanced ALD *J. Vac. Sci. Technol. A* **42** 033008
[20] Shih H-Y, Lee W-H, Kao W-C, Chuang Y-C, Lin R-M, Lin H-C, Shiojiri M and Chen M-J 2017 Low-temperature atomic layer epitaxy of AlN ultrathin films by layer-by-layer, *in-situ* atomic layer annealing *Sci. Rep.* **7** 39717
[21] Ueda S T *et al* 2022 Experimental and theoretical determination of the role of ions in atomic layer annealing *J. Mater. Chem. C* **10** 5707–15
[22] Lee W-H, Kao W-C, Yin Y-T, Yi S-H, Huang K-W, Lin H-C and Chen M-J 2020 Sub-nanometer heating depth of atomic layer annealing *Appl. Surf. Sci.* **525** 146615
[23] Kushner M J 2009 Hybrid modelling of low temperature plasmas for fundamental investigations and equipment design *J. Phys. D: Appl. Phys.* **42** 194013
[24] Kruger F, Lee H, Nam S K and Kushner M J 2023 Voltage waveform tailoring for high aspect ratio plasma etching of SiO_2 using $Ar/CF_4/O_2$ mixtures: consequences of ion and electron distributions on etch profiles *J. Vac. Sci. Technol. A* **41** 013006
[25] Litch E, Lee H, Nam S K and Kushner M J 2025 Consequences of low bias frequencies in inductively coupled plasmas on ion angular distributions for high aspect ratio plasma etching *J. Vac. Sci. Technol. A* **43** 033001
[26] Piskin T, Sriraman S, Lee H, Nam S K and Kushner M J 2025 Use of an auxiliary electrode to control plasma properties at the wafer edge in inductively coupled plasmas with a substrate bias *J. Vac. Sci. Technol. A* **43** 063001
[27] Scharfetter D L and Gummel H K 1969 Large-signal analysis of a silicon read diode oscillator *IEEE Trans. Electron Dev.* **16** 64–77
[28] Magboltz 8.97 database (available at: www.lxcat.net) (Accessed September 2011)
[29] Bogaerts A and Gijbels R 1999 Role of Ar^{2+} and $Ar_2{}^+$ ions in a direct current argon glow discharge: a numerical description *J. Appl. Phys.* **86** 4124–33
[30] Dwivedi A and Hara K 2025 Estimation of electron kinetics in low-temperature plasmas using data assimilation *J. Phys. D: Appl. Phys.* **58** 175203
[31] Godyak V A and Demidov V I 2011 Probe measurements of electron-energy distributions in plasmas: what can we measure and how can we achieve reliable results? *J. Phys. D: Appl. Phys.* **44** 233001

[32] Andreev S N, Bernatskiy A V, Dyatko N A, Kochetov I V, Lagunov V V and Ochkin V N 2023 Accounting for plasma resistance in the interpretation of probe measurements in gas discharge plasma *Vacuum* **215** 112372

[33] Lee H-C, Lee M-H and Chung C-W 2010 Experimental observation of the transition from nonlocal to local electron kinetics in inductively coupled plasmas *Appl. Phys. Lett.* **96** 041503

[34] Takao Y, Eriguchi K and Ono K 2012 Effect of capacitive coupling in a miniature inductively coupled plasma source *J. Appl. Phys.* **112** 093306

[35] Piejak R B, Godyak V A and Alexandrovich B M 1992 A simple analysis of an inductive RF discharge *Plasma Sources Sci. Technol.* **1** 179–86

[36] Walton S G, Foley B M, Tomko J, Boris D R, Gillman E D, Hernandez S C, Giri A, Petrova T B and Hopkins P E 2018 Plasma-surface interactions in atmospheric pressure plasmas: *in situ* measurements of electron heating in materials *J. Appl. Phys.* **124** 043301

[37] Godyak V A and Alexandrovich B M 2017 Power measurements and coupler optimization in inductive discharges *Rev. Sci. Instrum.* **88** 083512